A global deep-sea small protein atlas reveals a reservoir of noncanonical antimicrobial peptides

Qiuyun Jiang[1 #], Yingchun Han[1 #], Chenyang Ye[2 #], Yiqian Duan[3], Fang Li[1], Zhuang Han[4], Célio Dias Santos-Júnior[5,6], Zhouqing Luo[2 *], Xiyang Dong[1 *]

[1] Key Laboratory of Marine Genetic Resources, Third Institute of Oceanography, Ministry of Natural Resources, Xiamen 361005, China

[2] State Key Laboratory of Cellular Stress Biology, Innovation Center for Cell Signaling Network, School of Life Sciences, Xiamen University, Xiamen 361102, China

[3] Institute of Science and Technology for Brain-Inspired Intelligence, Fudan University, Shanghai 200433, China

[4] State Key Laboratory of Deep-Sea Science and Intelligent Technology, Institute of Deep-sea Science and Engineering, Chinese Academy of Sciences, Sanya 572000, China

[5] Hubei Hongshan Laboratory, Wuhan 430070, China

[6] College of Food Science and Technology, Huazhong Agricultural University, Wuhan 430070, China.

[#] These authors contributed equally to this work.

* Correspondence: dongxiyang@tio.org.cn (X.D.); luozq@xmu.edu.cn (Z.L.)

Abstract

Small proteins encoded by small open reading frames (smORFs; ≤ 100 aa) represent a largely unexplored dimension of microbial diversity, especially in the deep sea. By analyzing 708 metagenomes from five major deep-sea biomes (hadal trenches, cold seeps, hydrothermal vents, abyssal plains, and seamounts), we constructed the Deep-Sea Small Protein Atlas, comprising 88.7 million smORFs with exceptional novelty and strong habitat specificity. Deep-learning predictions identified 5.47 million candidate antimicrobial peptides (c_AMPs), revealing a peptide space far larger and structurally distinct from known AMPs. Deep-sea c_AMPs are longer, enriched in nonpolar and acidic residues, and exhibit low charge and high intrinsic disorder, suggesting non-membranolytic modes of action. We synthesized 131 representative peptides, of which 87% were antimicrobial, with MICs as low as 1.25 μM, broad-spectrum antibacterial and even antifungal efficacy, and minimal mammalian cytotoxicity. Transcriptomics, TEM imaging, and peptide–protein modeling showed that representative peptides preserve membrane integrity while disrupting intracellular processes such as translation and metabolism, supporting intracellular, non-lytic mechanisms. This work uncovers a vast reservoir of previously unrecognized deep-sea small proteins and structurally unconventional AMPs, providing a foundational resource for discovering next-generation peptide therapeutics.

Introduction

The deep sea, comprising cold seeps, hydrothermal vents, hadal trenches, abyssal plains, and seamounts, represents Earth's largest and least explored biome, extending below 200 meters and encompassing nearly three-quarters of the ocean's volume[1]. These environments are defined by extreme physicochemical conditions: perpetual darkness, low temperatures (0–4°C, except for hydrothermal systems that exceed 100°C), and immense hydrostatic pressure reaching up to 110 MPa in the deepest trenches. Such harsh conditions have driven the evolution of unique microbial communities with specialized physiological traits and metabolic architectures[1]. Deep-sea microorganisms are prolific producers of bioactive molecules that mediate competition and environmental adaptation, as exemplified by the discovery of unique biosynthetic gene clusters in cold-seep microbiome[2, 3]. Among these adaptations, small proteins encoded by small open reading frames (smORFs; ≤ 100 amino acids) have emerged as a particularly intriguing but underexplored molecular class[4]. Across diverse organisms, smORFs play critical roles in gene regulation[5], stabilization of large protein complexes[6], signal transduction[7], protein transport[8], stress responses[9], and antimicrobial defense[10]. Despite this functional breadth, the diversity, ecological distribution, and biological roles of smORFs in deep-sea ecosystems remain largely unknown.

Antimicrobial peptides (AMPs) represent one biologically important subset of smORF-encoded proteins. These peptides exhibit activity against bacteria, fungi, and viruses[10, 11], and are characterized by properties such as reduced propensity for resistance development[12, 13], increased target specificity, and often lower cytotoxicity compared with conventional antibiotics. However, the systematic discovery of AMPs has been historically constrained by technical limitations, including biased biochemical enrichment, incomplete mass spectrometry reference databases[14], and challenges in distinguishing genuine short coding sequences from spurious predictions[15]. Recent advances in ribosome profiling[16], proteomics[17], comparative genomics[18], and artificial intelligence[19] have transformed our ability to identify small proteins at scale. For

70 example, the Global Microbial Small Protein Catalog (GMSC) contains nearly one
71 billion non-redundant smORFs from 75 environments[4], while the AMPSphere database
72 reports 863,498 predicted AMPs, more than half of which show antimicrobial activity
73 upon synthesis[20]. Similar large-scale efforts in the human gut[19] and marine biofilms[21]
74 have further demonstrated the abundance and functional potential of environmental
75 AMPs. Yet, despite representing Earth's largest reservoir of microbial novelty[22, 23], the
76 deep sea remains conspicuously underrepresented in these global surveys. Most
77 existing studies rely on cultivation-dependent approaches[24-28], which capture only a
78 small fraction of deep-sea microbial diversity, leaving the vast majority of deep-sea
79 smORFs and AMP-like peptides unexplored.

80 AMPs operate through diverse mechanisms of action. Classical membrane-disruptive
81 pathways involve electrostatic interactions between cationic peptides and anionic
82 bacterial surface components such as lipopolysaccharides[29], followed by membrane
83 destabilization through barrel-stave, toroidal pore, or carpet-like mechanisms[30].
84 Increasing evidence, however, indicates that many AMPs act through non-
85 membranolytic mechanisms[31], including inhibition of cell-wall synthesis, replication,
86 transcription, translation, or other essential intracellular processes[32-34]. Such
87 mechanistic diversity expands the functional landscape of antimicrobial peptides and
88 offers opportunities to develop next-generation therapeutics with improved specificity
89 and reduced host toxicity[32]. Given the extreme physicochemical constraints of deep-sea
90 environments, it remains unclear whether deep-sea-derived AMPs follow classical lytic
91 paradigms or instead encode fundamentally distinct modes of action.

92 Here, we present the Deep-Sea Small Protein Atlas, a comprehensive resource that
93 systematically maps smORFs and antimicrobial peptides across five major deep-sea
94 biomes. By integrating large-scale metagenomic data with advanced computational
95 annotation and deep-learning-based peptide prediction, we construct non-redundant,
96 habitat-resolved smORF catalogs that uncover a vast and previously inaccessible
97 diversity of microbial small proteins and previously undescribed AMP candidates. We

98 further combine targeted peptide synthesis with antimicrobial assays, transcriptomics,
99 structural modeling, and ultrastructural imaging to interrogate the biological activities
100 and mechanistic potential of representative smORF-derived AMPs. Together, this atlas
101 establishes a foundational framework for understanding small-protein-mediated
102 adaptation in extreme environments and expands the structural and mechanistic
103 repertoire available for next-generation peptide therapeutics.

104 Results

105 A vast and previously uncharted deep-sea small-protein landscape

106 We constructed a large-scale atlas of microbial smORFs from 708 metagenomic
107 samples across five ecologically distinct deep-sea ecosystems **(Fig. 1a;**
108 **Supplementary Table 1)**. Within each ecosystem, smORFs (≤ 100 aa) were predicted
109 from assembled contigs using a unified workflow and subsequently dereplicated to
110 generate five non-redundant habitat-specific catalogs (**Methods; Fig. 1b**). In total, we
111 identified 88.7 million predicted smORFs, including 49.9 million from hadal trenches,
112 32.5 million from cold seeps, 3.8 million from hydrothermal vents, 0.8 million from
113 abyssal plains, and 1.8 million from seamounts, representing the most comprehensive
114 deep-sea small-protein resource available to date (**Supplementary Fig. 1;**
115 **Supplementary Table 2**).

116 Deep-sea smORFs exhibited exceptionally high novelty relative to existing reference
117 databases. On average, only 23.8% and 4.3% (range: 2.9–29.1%) of deep-sea smORFs
118 displayed detectable homology to entries in sORFdb[35] and SmProt[36], respectively **(Fig.**
119 **1c)**. Even when compared with GMSC[4], the largest microbial smORF dataset currently
120 available, an average of 26.8% (range: 19.3–34.9%) of deep-sea smORFs remained
121 unmatched. In total, 23.8 million smORFs showed no similarity to any tested database,
122 greatly expanding the known sequence space of small proteins. Functional and
123 taxonomic annotations further underscored this novelty. Approximately 53.6% (range:
124 47.8–59.2%) of smORFs lacked KEGG, eggNOG, CAZy, or Pfam annotations **(Fig.**

125 **1d; Supplementary Table 2)**, and nearly half (43.3%; range: 36.4–49.6%) could not
126 be assigned to any taxonomic lineage across the five ecosystems (**Supplementary Fig.**
127 **2**). In line with estimates that ~90% of deep-sea microbial taxa remain undescribed[22,
128 37], the Deep-Sea Small Protein Atlas provides a foundational resource for uncovering
129 previously unknown adaptive mechanisms, ecological functions, and bioactive
130 molecules within Earth's largest and least explored biosphere.

131 **Habitat specificity and distinct metabolic adaptations across deep-sea smORFs**

132 Environmental heterogeneity across the five deep-sea biomes imposes strong selective
133 pressures that shape the diversity and distribution of smORFs. Pairwise comparisons
134 showed that smORFs are overwhelmingly habitat-specific: on average, 86.4% (62.9–
135 97.8%) of smORFs were restricted to a single biome, whereas only 4.4% (0.1–35.0%)
136 were shared between any two habitats (**Fig. 2a; Supplementary Table 3**). Sharing was
137 lowest between hydrothermal vents and abyssal plains (0.1%), reflecting the sharp
138 ecological segregation associated with hydrothermal chemistry[38]. Consistently, within-
139 habitat sharing was minimal, with only 2.5% of smORFs shared in hadal trench samples,
140 2.2% in cold seeps, 4.7% in hydrothermal vents, 37.1% in abyssal plains, and 21.2% in
141 seamounts. The most physiochemically extreme habitats (hadal trenches, cold seeps,
142 and hydrothermal vents) harbored the highest proportions of unique smORFs (> 95.3%),
143 likely driven by steep redox gradients, high hydrostatic pressure, and strongly reducing
144 conditions[38-41]. By contrast, the more stable, oxygenated abyssal plains and seamounts[42,
145 43] exhibited comparatively higher levels of smORF sharing.

146 Despite this pronounced habitat specialization, the atlas revealed a conserved core of
147 902 smORFs present across all biomes (**Supplementary Table 4**). Functional
148 annotation showed enrichment in essential cellular processes, including translation,
149 ribosomal structure and biogenesis (25.8%), transcription (19.1%), and energy
150 production and conversion (10.1%) (**Fig. 2b; Supplementary Table 5**). These findings
151 highlight a dual organizational structure within the deep-sea smORFome: a vast, highly
152 specialized set of habitat-restricted smORFs shaped by localized selection pressures,

153 and a small, deeply conserved core required for fundamental cellular processes across
154 extreme physicochemical regimes.

155 Taxonomic profiling further underscored this pattern of habitat structuring while
156 revealing remarkable phylogenetic breadth. Using MMseqs2-based classification[44]
157 with GTDB R220 [45], 46,303,778 smORFs were taxonomically assigned, spanning 18
158 archaeal and 169 bacterial phyla (**Supplementary Table 6**). Over half of all annotated
159 smORFs were species-specific, with 81.8–89.7% of archaeal and 62.0–68.8% of
160 bacterial assignments mapping to species-level lineages (**Supplementary Fig. 3**).
161 Distinct habitat-level taxonomic signatures were evident: *Nitrososphaeria* dominated
162 archaeal smORFs in hadal trenches (38.0%), abyssal plains (79.3%), and seamounts
163 (89.9%), whereas *Methanosarcinia* (22.0%) and *Thermoprotei* (14.6%) predominated
164 in cold seeps and hydrothermal vents, respectively (**Fig. 2c; Supplementary Table 7**).
165 Among bacteria, *Alphaproteobacteria* were most abundant in hadal trenches (15.2%)
166 and abyssal plains (17.4%), while *Gammaproteobacteria* predominated in cold seeps
167 (12.5%), hydrothermal vents (15.5%), and seamounts (19.7%). These lineage-specific
168 patterns are consistent with known biogeographic distributions[41, 43, 46] and reflect
169 microbial adaptation to highly contrasting redox, pressure, and energy landscapes.
170 Collectively, the atlas demonstrates how local physicochemical regimes act as
171 dominant selective forces shaping the evolution, diversification, and ecological
172 partitioning of small proteins across the deep-sea biosphere[39, 47-49].

173 Functional annotation further revealed metabolic specializations that distinguish deep-
174 sea smORFs from global small-protein repertoires. On average, 46.4% of smORFs per
175 habitat were assigned to COG categories[50] (37.7 million total; **Supplementary Table**
176 **2**). Among these, ~20.5% belonged to poorly characterized functions (S), highlighting
177 the deep sea as a rich reservoir of uncharacterized protein functions. Annotated
178 smORFs were enriched in categories C, J, K, E, and L, corresponding to energy
179 metabolism, amino acid metabolism, and core informational processes
180 (**Supplementary Figs. 4-5; Supplementary Table 8**). Consistent with GMSC

181 database[4], information-processing functions constituted a major fraction of annotated
182 smORFs; however, the disproportionate representation of metabolic categories
183 distinguishes the deep-sea smORFome from global trends[4] and highlights the role of
184 smORFs in mediating physiological adaptation to extreme environments[1, 3].

185 Protein feature analysis showed that ~12.6% of smORFs encode transmembrane helices
186 and ~1.6% contain signal peptides (**Fig. 2d; Supplementary Table 9**), suggesting that
187 membrane-associated or secreted small proteins are widespread. These features were
188 more common in bacterial than archaeal smORFs (**Supplementary Fig. 6**), likely
189 reflecting both limited characterization of archaeal secretion systems and distinct
190 ecological strategies. Approximately 1.1% of smORFs encoded Sec/Tat signal peptides
191 and 0.5% encoded lipoprotein signal motifs **(Supplementary Fig. 7**), consistent with
192 roles in cell–cell communication, nutrient acquisition, syntrophy, or environmental
193 sensing[5, 51, 52]. Together, these findings reveal a deep-sea smORF repertoire enriched in
194 metabolic and secreted functions that support microbial survival, interaction, and
195 ecosystem functioning under extreme conditions.

196 **Unconventional, structurally flexible, and uncharacterized deep-sea c_AMPs**

197 Using four independent deep-learning-based prediction tools, we identified 5,469,335
198 candidate antimicrobial peptides (c_AMPs) from the Deep-Sea Small Protein Atlas
199 (**Supplementary Fig. 8**). This represents an expansion of ~152-fold and ~1,654-fold
200 relative to the experimentally validated AMPs in DRAMP v4.0 [53] and APD v3 [54],
201 respectively. The deep-sea repertoire also exceeds computationally predicted AMP
202 collections by ~6-fold (AMPSphere[20]), ~127-fold (encrypted peptides (EPs) from the
203 human proteome[55]), and ~16,039-fold (marine biofilm-derived AMPs[21]). Sequence-
204 level homology was minimal: only 0.03% and 0.21% of deep-sea c_AMPs showed
205 similarity to DRAMP or APD entries, respectively (**Fig. 3a**). On average, 96.25% of
206 c_AMPs were absent from all three major computational AMP resources (AMPSphere,
207 EPs, and marine biofilms), and overall fewer than 14.32% had detectable homology to
208 any known peptide. These results reveal a largely unexplored antimicrobial sequence

space with substantial biotechnological potential.

Amino acid composition profiling uncovered a distinct biochemical signature. Deep-sea c_AMPs were enriched in A (alanine), D (aspartic acid), E (glutamic acid), N (asparagine), Q (glutamine), S (serine), and T (threonine), but depleted in C (cysteine), K (lysine), R (arginine), and W (tryptophan) relative to DRAMP, APD, EPs and marine biofilm datasets (**Fig. 3b; Supplementary Table 10**). The enrichment of acidic residues (D, E) contrasts sharply with canonical membrane-disruptive AMPs, typically cationic and enriched in K and R that facilitate electrostatic interactions with negatively charged microbial membranes[20, 21, 55], suggesting that these peptides likely employ fundamentally different interaction modes with microbial cells. Correspondingly, deep-sea c_AMPs exhibited near-neutral net charge (~0 at pH 7) and substantially lower isoelectric points (pI ~7) compared with reference AMPs (+2 to +7; pI 9–11.5, $P < 0.0001$; **Fig. 3c; Supplementary Tables 11–12**). Such electrostatic profiles imply a reduced dependence on charge-mediated membrane disruption, instead pointing toward alternative mechanisms, including metal ion coordination, protein–protein interaction, or intracellular pathway modulation[56-58].

Multiple residue-level features further support a shift toward noncanonical structural paradigm. Elevated alanine content (**Fig. 3b**) suggests a bias toward flexible, low-complexity scaffolds[59], whereas marked cysteine depletion reduces reliance on disulfide-stabilized β-sheet structures, favoring linear or intrinsically disordered conformations[60]. Predicted structural ensembles showed predominantly extended coils with short, transient α-helical segments (**Fig. 3d**), consistent with increased conformational plasticity. Such structural flexibility has been linked to non-membrane-disruptive antimicrobial modes, including selective intracellular targeting and specific molecular recognition[61, 62]. These observations align with our TEM imaging and transcriptomic analyses (see below), which showed antimicrobial activity without classical membrane permeabilization.

Physicochemical profiling reinforced the unique nature of deep-sea c_AMPs. They

237 were longer (~67 aa) and heavier (~7 kDa) than reference AMPs (17–29 aa; 2–4 kDa),
238 showed moderate hydrophobicity (GRAVY ≈ 0.01 vs. −0.30 to −0.47), and exhibited
239 significantly reduced hydrophobic moments (~0.38 vs. 0.72–0.77; $P < 0.0001$),
240 indicative of weak α-helical amphipathicity (**Supplementary Fig. 9; Supplementary**
241 **Tables 11–12**). Deep-sea peptides also displayed higher disorder propensity, enhanced
242 polyproline II (PPII) tendency, and greater linear moment values ($P < 0.05$; **Fig. 3c;**
243 **Supplementary Fig. 9**), features associated with increased structural flexibility, which
244 may expand the repertoire of potential molecular targets. Reduced amphiphilicity and
245 net charge could also decrease nonspecific cytotoxicity, a beneficial trait for therapeutic
246 peptides. Together, these findings suggest that deep-sea c_AMPs represent a previously
247 unrecognized class of antimicrobial peptides, characterized by low charge, intrinsic
248 disorder, conformational adaptability, and diminished amphipathicity.

249 **Broad-spectrum antibacterial and antifungal activity with minimal cytotoxicity**

250 To experimentally validate computational predictions in the Deep-Sea Small Protein
251 Atlas, we synthesized 131 representative c_AMPs and evaluated their antimicrobial
252 properties. Each peptide was screened at 125 μM, a benchmark concentration
253 commonly used in AMP discovery studies[19], against nine representative
254 microorganisms, including Gram-positive bacteria (*Priestia filamentosa* and
255 *Staphylococcus aureus* RN450), Gram-negative bacteria (*Escherichia coli* DH5α, *E.*
256 *coli* BW25113, *Klebsiella pneumoniae* ATCC 13883, *Vibrio parahaemolyticus*
257 VP.1997, *Halomonas bluephagenesis* TD01, and *Acinetobacter pittii*), and the yeast
258 *Saccharomyces cerevisiae* BY4741. A total of 114 peptides (87.0%) inhibited the
259 growth of at least one microorganism (**Supplementary Fig. 10; Supplementary Table**
260 **13**), demonstrating an exceptionally high validation rate compared with previous AMP
261 discovery efforts.

262 Minimum inhibitory concentration (MIC) assays identified several highly potent
263 peptides, including plain-4/sm-4, hydrothermal vent-19, and hydrothermal vent-35,
264 with activities down to 1.25 μM, comparable to the positive controls nisin and melittin[63,

265 [64] (**Fig. 4a; Supplementary Tables 14–15**). Susceptibility varied across strains, with
266 the highest numbers of active peptides observed for *P. filamentosa* (38 hits), *H.*
267 *bluephagenesis* (31), *A. pittii* (16), and *S. aureus* (12). Several peptides displayed broad-
268 spectrum properties, including 22/131 active against both Gram-positive and Gram-
269 negative species and 7/131 active across multiple species within the same Gram group
270 (**Supplementary Table 15**). Representative c_AMPs achieved complete bactericidal
271 activity (≥ 99.9% killing) at 1 × – 4 × MIC against *P. filamentosa*, *H. bluephagenesis*,
272 *V. parahaemolyticus*, *A. pittii*, and *E. coli* DH5*α* **(Fig. 4b; Supplementary Figs. 11–**
273 **13; Supplementary Table 16**), confirming strong and reproducible antimicrobial
274 efficacy.

275 Consistent with ecological expectations, no c_AMPs inhibited *S. cerevisiae* under
276 fermentative conditions (YPD), potentially reflecting weaker evolutionary pressure to
277 target fungi, an infrequent component of deep-sea communities (< 1–4%)[65, 66].
278 However, subtle growth defects emerged during the ethanol-dependent secondary
279 growth phase (**Supplementary Fig. 14**). Under respiratory conditions (YPEG; ethanol
280 + glycerol), cold seep-38 displayed strong antifungal activity (MIC = 8 μM) (**Fig. 4a**).
281 Because ethanol metabolism requires functional mitochondria, these observations
282 suggest that cold seep-38 may interfere with mitochondria-associated pathways,
283 consistent with downstream transcriptomic responses described below.

284 To evaluate biosafety, we assessed eight deep-sea c_AMPs (hadal trench-22, cold seep-
285 3, cold seep-9, cold seep-38, hydrothermal vent-9, hydrothermal vent-19, hydrothermal
286 vent-36, and plain-4/sm-4) in mammalian cell lines, including a non-tumorigenic line
287 (HEK293T) and two cancer lines (HepG2, HeLa). All peptides exhibited low
288 cytotoxicity, with no significant dose-dependent effects observed in HeLa cells across
289 the tested concentration range (**Fig. 4c; Supplementary Table 17**). The cold seep-9
290 showed mild dose-dependent toxicity toward HEK293T cells, whereas cold seep-38
291 displayed stronger, cell line–specific effects in HEK293T and HepG2 but minimal
292 impact on HeLa cells. Given the differing energy demands and mitochondrial

293 abundance across these cell types[67], this cell line–specific response suggests that its
294 activity may be linked to cellular energy metabolism and particularly mitochondria
295 related function[68], consistent with the antifungal assays[68].

296 **Diverse but predominantly non-lytic, intracellular antimicrobial strategies**

297 Mechanistic profiling of representative deep-sea–derived c_AMPs revealed a coherent
298 signature across peptides and taxa, most notably cold seep-9, hydrothermal vent-19,
299 and cold seep-38, which showed the strongest *in vitro* activity against *A. pittii*, *P.*
300 *filamentosa*, *V. parahaemolyticus*, and *S. cerevisiae*. Despite their structural diversity
301 and the phylogenetic differences of the target organisms, these peptides consistently
302 induced non-lytic antimicrobial responses characterized by modest perturbation of
303 membrane permeability and pronounced intracellular effects on translation,
304 proteostasis, and metabolic homeostasis, rather than catastrophic membrane lysis. To
305 dissect these mechanisms, we performed transcriptomic profiling following AMP
306 exposure, a widely used strategy for resolving intracellular targets and stress
307 responses[31, 69]. Based on MIC results (**Fig. 4**), we selected four peptide–microbe
308 combinations: *A. pittii* treated with cold seep-9 (MIC = 5 μM), *P. filamentosa* treated
309 with hydrothermal vent-19 (MIC = 1.25 μM), *V. parahaemolyticus* treated with
310 hydrothermal vent-19 (MIC = 1.25 μM), and *S. cerevisiae* treated with cold seep-38
311 (MIC = 8 μM). Across all organisms, only a restricted number of genes were
312 significantly altered (|log2FC| ≥ 1 for bacteria, ≥ 0.5 for yeast; FDR < 0.05; **Fig. 5a**),
313 consistent with targeted rather than global stress responses. DEG counts ranged from
314 127 in *A. pittii* to only 13 in *S. cerevisiae* (**Supplementary Tables 18-21**), reflecting
315 organism- and pathway-specific peptide sensitivity.

316 In *A. pittii*, 120 of 127 DEGs were associated with metabolic pathways
317 (**Supplementary Fig. 15a; Supplementary Table 18**). Carbon metabolism (21 DEGs)
318 and amino acid metabolism (19 DEGs) were prominently affected. Two pathways
319 showed the strongest perturbation: benzoate degradation (13/35 genes; **Supplementary**
320 **Fig. 15a, 16b**) and branched-chain amino acid degradation (9/28 genes;

321 **Supplementary Fig. 15a, 16c**). GO enrichment **(Fig. 5b)** highlighted a strong
322 overrepresentation of membrane-localized proteins, particularly those associated with
323 the cell envelope and transport processes. The transporters comprised systems
324 mediating the uptake or export of carbon sources (e.g., *quiX*), amino acids (including
325 multiple MFS and DMT family transporters), and ions (e.g., members of the RcnB
326 family (**Supplementary Table 18**). Although cold seep-9 lacks predicted
327 transmembrane helices (**Supplementary Fig. 16d**), AlphaFold3 modeling suggested a
328 physically plausible interaction with an ABC transporter permease (ipTM = 0.67, pTM
329 = 0.73; **Fig. 5c**), pointing to a mechanism involving modulation of membrane-
330 associated transport rather than membrane insertion. Collectively, these findings
331 suggest that cold seep-9 modestly perturbs membrane permeability, leading to
332 disruption of carbon, nitrogen, and ion homeostasis and broadly impairing metabolic
333 balance.

334 In *P. filamentosa*, translation-related genes were strongly downregulated (28/57
335 ribosomal genes), alongside genes involved in flagellar assembly (15/35) (**Fig. 5d;**
336 **Supplementary Fig. 15b; Supplementary Table 19**). Both large and small ribosomal
337 subunits exhibited extensive downregulation (**Fig. 5e**). Aminoacyl-tRNA ligases (*thrS*
338 etc), tRNA-modifying enzymes (including *truA* and *truB*), and aminotransferases (*gatC*)
339 were also repressed (**Supplementary Table 19**), indicating substantial impairment of
340 translational capacity. AlphaFold3 modeling predicted a high-confidence interaction
341 between hydrothermal vent-19 and TruA (ipTM = 0.87, pTM = 0.90), a key tRNA
342 pseudouridine synthase (**Fig. 5f**), providing a mechanistic basis for translation
343 inhibition. Altogether, these results suggest that hydrothermal vent-19 likely exerts its
344 antibacterial activity primarily by disrupting protein translation, thereby impairing
345 multiple cellular processes including flagellum biogenesis, ultimately compromising
346 bacterial viability. Consistent with the well-documented flagellar shedding phenotype
347 observed following AMP treatment[70], TEM imaging revealed flagellar loss in
348 hydrothermal vent-19–treated cells (**Fig. 5g**). Additional AMPs exhibited distinct
349 phenotypes: cold seep-32 caused cell enlargement with pale cytoplasmic density,

350 whereas cold seep-37 induced elongation and cytoplasmic leakage, highlighting
351 mechanistic diversity among deep-sea peptides.

352 In *V. parahaemolyticus*, hydrothermal vent-19 triggered upregulation of ribosomal
353 genes (17/56) and components of the bacterial secretion system (12/58) (**Fig. 5h;**
354 **Supplementary Fig. 14c; Supplementary Table 20**), critical for virulence[71]. This
355 response contrasts with the downregulation observed in Gram-positive *P. filamentosa*,
356 suggesting that organism-specific regulatory architectures shape transcriptional outputs
357 despite potentially shared molecular targets. Supporting this, hydrothermal vent-19 also
358 displayed a predicted interaction with TtcA (ipTM = 0.8, pTM = 0.84; **Fig. 5i**), a tRNA
359 thiolation enzyme involved in tRNA modification that contributes to efficient
360 translation, particularly under stress conditions. Together, these data indicate that
361 hydrothermal vent-19 primarily targets translation machinery, with downstream
362 consequences that differ between Gram-positive and Gram-negative bacteria.

363 The limited DEGs in *S. cerevisiae* (n = 13; $|\log2FC| \geq 0.5$, FDR < 0.05; **Supplementary**
364 **Fig. 15d; Supplementary Table 21)** is consistent with the observation that cold seep-
365 38 treatment resulted in only slight growth reduction during the secondary growth phase
366 in YPD, when ethanol becomes the primary carbon source **(Supplementary Figs. 14,**
367 **15d)**. The complete growth inhibition under YPGE condition **(Fig. 4a)** prompted us to
368 further investigate potential transcriptional changes, revealing that cold seep-38 induces
369 mild rather than extensive transcriptional perturbation. KEGG enrichment revealed
370 perturbation of carbon and energy metabolism, with *PCK1*, a key gluconeogenic and
371 ethanol-utilization gene (**Supplementary Figs. 15d, 17**), significantly downregulated.
372 Removal of the peptide fully restored respiratory growth (**Supplementary Fig. 18**),
373 indicating a reversible inhibitory mechanism. The peptide's cell-line–specific
374 cytotoxicity (**Fig. 4c**) further supports a connection to mitochondrial or energy-linked
375 processes, raising the possibility that cold seep-38 may function as a reversible
376 modulator of central carbon metabolism with broader implications for
377 immunometabolism and cancer biology (**Supplementary Fig. 19**).

Discussion

This study provides three conceptual advances: (i) the first global atlas of deep-sea small proteins; (ii) the discovery of a structurally distinct class of noncanonical c_AMPs; and (iii) experimental evidence that representative peptides act predominantly through intracellular, non-lytic mechanisms. The Deep-Sea Small Protein Atlas uncovers an expansive and previously inaccessible repertoire of bioactive peptides, over 85% of which show no detectable similarity to existing AMP databases, greatly expanding the known sequence space of natural antimicrobials. Representative c_AMPs demonstrated broad antimicrobial efficacy across Gram-positive and Gram-negative bacteria and even a mitochondrial-dependent yeast strain, suggesting that their primary targets may lie beyond the cell membrane. Such breadth of activity is consistent with mechanisms that are not strictly dependent on membrane composition[32]. Indeed, transcriptomic analyses revealed perturbations in translation, proteostasis, and metabolic pathways rather than gene expression patterns characteristic of classical membrane lysis, indicating that intracellular pathways are likely the dominant targets of these peptides under deep-sea environmental conditions such as high hydrostatic pressure, extreme temperature, and nutrient limitation.

A distinctive feature of the deep-sea c_AMPs is their predicted intrinsic disorder. Unlike canonical AMPs that fold into amphipathic α-helices, these peptides appear structurally plastic, favoring extended or low-complexity conformations. Intrinsically disordered peptides can undergo environment-dependent structural transitions[72] and may interact with membranes through transient, peripheral contacts rather than inserting into bilayers to form stable pores. The behavior of cold seep-9 exemplifies this: despite lacking predicted transmembrane helices, it alters membrane permeability sufficiently to disrupt carbon, nitrogen, and ion homeostasis while maintaining overall membrane integrity. Analogous to disordered C-terminal motifs in endocytic adaptors, which generate steric pressure to drive membrane curvature[73], deep-sea peptides may exert functional effects without requiring stable secondary structure.

406 Functionally, representative c_AMPs inhibited diverse microorganisms, yet TEM
407 imaging revealed no evidence of catastrophic membrane damage. Cells maintained
408 intact envelopes but exhibited altered intracellular organization and transcriptional
409 responses. These observations contrast sharply with membrane-disruptive AMPs, such
410 as polymyxins and many amphipathic helical peptides[19, 20], which kill by compromising
411 membrane integrity. While membrane lysis is effective, it often correlates with
412 cytotoxicity in mammalian cells[74] due to nonspecific interactions with eukaryotic
413 membranes. In contrast, several antimicrobial peptides can cross membranes without
414 causing detectable damage and modulate intracellular processes[32], an emerging but still
415 poorly understood antimicrobial strategy. The deep-sea peptides characterized here
416 appear to fall within this underexplored mechanistic class.

417 Together, these findings reveal a vast diversity of previously uncharacterized small
418 proteins encoded by extreme marine ecosystems. The c_AMPs uncovered here possess
419 a unique combination of low net charge, intrinsic disorder, structural plasticity, and
420 intracellular, non-lytic mechanisms of action, collectively expanding the conceptual
421 landscape of natural antimicrobial strategies. These results challenge the prevailing
422 emphasis on membrane-disruptive paradigms and suggest that environmental extremes
423 such as those in the deep sea may drive the evolution of fundamentally distinct
424 antimicrobial modalities.

425 At the same time, our mechanistic analyses were restricted to a subset of short,
426 synthesizable peptides, and it remains unknown whether longer or more complex
427 c_AMPs share similar structural or mechanistic properties. Future work will require
428 pinpointing precise intracellular targets, determining peptide–protein interaction
429 structures at atomic resolution, exploring functional diversity across peptide families,
430 and evaluating pharmacokinetics and therapeutic potential *in vivo*. By enabling
431 systematic discovery and mechanistic exploration, the Deep-Sea Small Protein Atlas
432 provides a foundational resource for identifying next-generation peptide antibiotics
433 inspired by Earth's most remote and evolutionarily unique environments.

434 # Materials and Methods

435 ## Metagenomic dataset and processing

436 Metagenomic datasets included 308 samples (40 water samples and 268 sediment
437 samples) from hadal trenches in the Pacific Ocean (Mariana, Kermadec, Atacama, Kuril,
438 Izu-Bonin, and Japan Trenches), 174 cold seep sediment samples collected from 17
439 globally distributed seep sites, 160 hydrothermal vent samples (three hydrothermal
440 chimney samples, seven rock samples, 28 microbial mat samples, 38 water samples,
441 and 84 sediment samples) from the Pacific, Atlantic, Indian, and Arctic Oceans
442 (Brothers Volcano, Guaymas Basin, Juan de Fuca Ridge, Gakkel Ridge, Manus Basin,
443 the Southern Mariana Trough, and the Mid Cayman Rise), 56 seamount sediment
444 samples from the Pacific Ocean (Northwest Pacific Ocean, Takuyo-Daigo Seamount,
445 Takuyo-Daisan Seamount, and seamounts along the Yap and Mariana trenches), and 10
446 abyssal plain sediment samples from the Pacific Ocean **(Supplementary Fig. 1a and**
447 **Supplementary Table 1)**. A total of 115 cold seep sediment metagenomic datasets were
448 generated by our group and reported in our previous publications[23, 75-82], whereas the
449 remaining datasets were retrieved from the National Center for Biotechnology
450 Information Sequence Read Archive (NCBI-SRA) and the European Bioinformatics
451 Institute European Nucleotide Archive (EBI-ENA). Detailed information, including
452 associated publications, sample metadata, sequencing platforms, and accession
453 numbers, is provided in **Supplementary Table 1**. For each sample, metagenomic reads
454 were quality-filtered using fastp[83] (v0.23.2, default parameters), and clean reads were
455 assembled using MEGAHIT[84] (v1.2.9, default parameters). In total, 1,058,734,804
456 contigs were generated (> 200 bp), including 807,712,620 from hadal trenches,
457 59,011,641 from cold seeps, 125,126,723 from hydrothermal vents, 15,953,963 from
458 abyssal plains, and 50,929,857 from seamounts (**Fig. 1b and Supplementary Table 2**).
459 All assembled contigs were used for subsequent smORF prediction.

460 **Non-redundant smORF catalog construction and cross-habitat analyses**

461 smORFs were predicted from assembled contigs using smorFinder[85] (v1.0.0, default
462 parameters) and GMSC-mapper[4] (v0.0.1a0, parameters: --no-habitat --no-taxonomy).
463 The predicted smORFs were first deduplicated at 100% amino acid identity and 100%
464 coverage using CD-HIT[86] (v4.8.1, parameters: -c 1 -aS 1 -g 1 -d 0). All non-singleton
465 sequences were subsequently clustered at 90% amino acid identity and coverage with
466 MMseqs2 (v13.45111)[87] using the easy-linclust module (parameters: -c 0.9 -min-seq-
467 id 0.9). Singletons removed during the 100% identity deduplication step were further
468 evaluated to retain potentially meaningful homologs. These sequences were aligned
469 against MMseqs2 cluster representatives using DIAMOND[88] (v2.1.8, parameters: --id
470 90 --query-cover 90 --subject-cover 90 -e 1e-5). Homologous singletons were merged
471 with the MMseqs2 cluster representatives to generate the final non-redundant smORF
472 catalogs for each deep-sea habitat. The overall workflow is summarized in **Fig. 1b**. To
473 assess smORF sharing across habitats, pairwise comparisons between smORF catalogs
474 were performed using DIAMOND (v2.1.8, parameters: --id 100 --query-cover 100 --
475 max-target-seqs 1). smORFs with hits meeting this criterion were considered shared.

476 **Taxonomic and functional annotation of smORFs**

477 Taxonomic assignment of smORFs was performed using MMseqs2 [44] (v13.45111,
478 taxonomy module; parameter: --tax-lineage 1) against the GTDB reference database[45]
479 (R220). Functional annotation was conducted using eggNOG-mapper[89] (v2.1.9, default
480 parameters), based on eggNOG 5.0 orthology predictions and integrated databases
481 including Pfam 33.1, KEGG, EC numbers, GO terms, and CAZy families[90]. Given the
482 short length of smORFs, these eggNOG-based functional assignments should be
483 interpreted as tentative annotations. Signal peptides were predicted with SignalP 6.0
484 (default model) [91], which identifies classical Sec/SPI signal peptides (SP), twin-arginine
485 translocation (TAT) signals, lipoprotein signal peptides (LIPO and TATLIPO), and
486 PILIN (Sec/SPIII), a specialized class of Sec pathway signal peptides. Transmembrane

487 helices were predicted with TMHMM[92] (v2.0, default parameters), allowing the
488 determination of their number and topology.

489 **AMP prediction and physicochemical feature analysis**

490 AMPs were predicted by ampir (https://ampir.marine-omics.net/; precursor peptide
491 model), Macrel[93] (v 1.5.0, default parameters), amPEPpy[94] (v 1.1.0, parameter: --seed
492 2012), and AMPLify[95] (v 2.0.0, parameter: -m imbalanced). Any peptide predicted as
493 an AMP by at least one method was retained, and the combined outputs were merged
494 to generate a comprehensive c_AMP catalog for each habitat. The amino acid
495 composition of deep-sea c_AMPs was compared with experimentally validated AMPs
496 from DRAMP[53] (v4) and APD3 [54], as well as predicted datasets including AMPSphere[20],
497 EPs from the human proteome[55], and AMPs identified from marine biofilms[21].
498 Additional physicochemical features were computed using custom Python scripts
499 (Figshare: https://doi.org/10.6084/m9.figshare.30692342), including peptide length,
500 molecular weight, isoelectric point (pI), net charge at pH 7 (NetCharge_pH7), GRAVY
501 (grand average of hydropathy), amphiphilicity index, hydrophobic moment, linear
502 moment, polyproline II (PPII) propensity, and disorder propensity. For visualization,
503 2,000 AMPs were randomly selected from each habitat-specific catalog and each
504 reference database.

505 **Protein structure and peptide-protein interaction prediction**

506 Three-dimensional structures of 131 selected c_AMPs were predicted using
507 AlphaFold[96] (v2.0; parameter: full_dbs), and model confidence was evaluated using
508 pLDDT scores. Peptide–protein complex structures (targets: tRNA modifying enzymes
509 TruA and TtcA) were generated using AlphaFold3 [97], and prediction quality were
510 assessed using ipTM and pTM scores. All structural models were visualized and
511 exported as images using PyMOL (http://www.pymol.org).

512 **Assessment of deep-sea smORF and c_AMP novelty**

513 Each smORF catalog was compared against established small-protein reference
514 databases, including sORFdb[35], SmProt 2 [36], and GMSC[4], to evaluate the homology
515 and novelty of the identified deep-sea smORFs. Deep-sea c_AMPs were additionally
516 compared with experimentally validated AMPs from DRAMP[53] and APD3 [54], as well
517 as predicted AMP datasets including AMPSphere[20], EPs[55], and marine biofilm AMPs
518 [21]. All pairwise comparisons were performed using DIAMOND[88] (v2.1.8, parameters:
519 --more-sensitive --evalue 1e-5).

520 **Deep-sea c_AMP selection for synthesis and testing**

521 A total of 131 c_AMPs from the five deep-sea habitats were synthesized by solid-phase
522 peptide synthesis using the Fmoc strategy by Sangon Biotech (Shanghai) Co., Ltd.
523 Peptide molecular weights were verified by mass spectrometry, and purity (> 90%) was
524 confirmed by high-performance liquid chromatography. The selection criteria for these
525 peptides are described below.

526 Deep-sea c_AMPs were initially filtered by peptide length, excluding sequences longer
527 than 40 amino acids, as conventional Fmoc-based solid-phase peptide synthesis often
528 yields lower efficiencies and requires repeated recoupling steps for longer peptides[98, 99].
529 Two complementary groups of c_AMPs were then selected for downstream synthesis
530 and functional testing: (i) peptides predicted to have high antimicrobial potential, and
531 (ii) peptides randomly selected to represent taxonomic diversity across habitats. For the
532 first group, we employed EvoGradient[100] to predict and virtually evolve candidate
533 bioactive peptides, an explainable deep learning framework integrating convolutional
534 neural network (CNN)[101], long short-term memory networks (LSTM)[102], attention
535 networks[103] and Transformer models[103]. Peptides with high predicted antimicrobial
536 activity were subsequently filtered based on solubility (> 0.5) using the criteria
537 implemented in Protein–Sol[104]. This resulted in the selection of five peptides from
538 abyssal plains, five from seamounts (one overlapping with the abyssal plain group), 16

539 from cold seeps, 18 from hydrothermal vents, and 18 from hadal trenches (one
540 overlapping with the abyssal plain group). For the second group, c_AMPs were selected
541 according to their taxonomic classification at a defined rank to ensure representation
542 across taxonomic levels, retaining at least one peptide per rank. This yielded five
543 c_AMPs from abyssal plains, four from seamounts, 21 from cold seeps, 21 from
544 hydrothermal vents, and 20 from hadal trenches (one overlapping with the abyssal plain
545 group).

546 **Bacterial and fungal inhibition experiment**

547 Nine representative strains were selected for initial antimicrobial screening, including
548 Gram-positive bacteria *P. filamentosa* and *S. aureus* (ATCC RN450); Gram-negative
549 bacteria *E. coli* strains (DH5*α* and BW25113), *K. pneumoniae* (ATCC 13883), *V.*
550 *parahaemolyticus* (VP.1997; ATCC 17802), *H. bluephagenesis* (TD01), and *A. pittii*;
551 and the yeast *S. cerevisiae* (BY4741). Strains were streaked onto Luria–Bertani (LB)
552 agar medium and incubated overnight at 37°C, except *H. bluephagenesis,* which was
553 cultured on LB agar supplemented with 6 × NaCl (60 g L^{-1} NaCl); *S. aureus*, which
554 was grown on Mueller–Hinton (MH) agar; and *S. cerevisiae*, which was grown on yeast
555 extract–peptone–dextrose (YPD) agar at 30°C. Single colonies were inoculated into
556 appropriate liquid media and cultured overnight at 220 r.p.m. (37°C for bacteria; 30°C
557 for *S. cerevisiae*). Overnight bacterial cultures were diluted 1:100 (v/v) into fresh
558 medium and grown for 3 h to mid-exponential phase; *S. cerevisiae* cultures were diluted
559 to an OD_{600} of 0.1 and grown for 6 h to reach mid-exponential phase. Bacterial
560 suspensions were adjusted to an OD_{600} of 0.0002, and *S. cerevisiae* suspensions were
561 adjusted to an OD_{600} of 0.02 (≈ 2×10^5 CFU mL^{-1} in YPD or yeast extract–peptone–
562 ethanol–glycerol (YPEG) medium) and used as inocula for testing 131 synthesized
563 c_AMPs.

564 Freeze-dried c_AMPs was dissolved in double-distilled water to 0.4 mmol L^{-1}. Three
565 experimental groups were established in 96-well plates: (1) blank control, 100 μL fresh
566 medium; (2) microbial control, 50 μL fresh medium and 50 μL bacterial or yeast

567 suspension; and (3) c_AMPs treatment, 50 μL microbial suspension and 50 μL c_AMP
568 solution (final concentration 125 μmol L^{-1}). Each well contained a final volume of 100
569 μL and a microbial density of 1×10^5 CFU mL^{-1}. Plates were incubated at 37°C for
570 bacteria (30°C for *S. cerevisiae*) with shaking at 220 r.p.m for 16 h. OD_{600} values were
571 normalized by $(OD_{600,\ experiment} - OD_{600,\ blank}) / (OD_{600,\ control} - OD_{600,\ blank})$. The c_AMPs
572 were considered effective if they reduced bacterial or yeast growth by > 75% relative
573 to controls. All assays were performed with three biological replicates, each including
574 three technical replicates.

575 **Minimum inhibitory concentration determination**

576 MICs of c_AMPs were determined by the broth microdilution method[19]. Briefly,
577 microbial inocula were prepared as described for the inhibition experiment. A twofold
578 serial dilution of each c_AMP (160–2.5 μM) was prepared in fresh medium, and 50 μL
579 of each dilution was mixed with 50 μL of microbial inoculum in 96-well plates,
580 resulting in final peptide concentrations ranging from 80 to 1.25 μM and a microbial
581 density of 1×10^5 CFU mL^{-1}. Wells containing medium only (blank control) and
582 microbial cultures without peptide (growth control) were included on each plate. The
583 MIC was defined as the lowest peptide concentration with no detectable growth after
584 16 h incubation (37°C for bacteria; 30°C for *S. cerevisiae*). All assays were performed
585 in triplicate with three independent biological replicates.

586 **Minimum bactericidal concentration determination**

587 Minimum bactericidal concentrations (MBCs) of bioactive c_AMPs were determined
588 according to the European Committee on Antimicrobial Susceptibility Testing
589 (EUCAST) guidelines for bactericidal activity assessment. Briefly, bacterial cultures
590 were prepared as described for MIC determination. After 16 h exposure to c_AMPs, 50
591 μL of culture from each well was spread onto LB agar plates lacking antimicrobial
592 agents and incubated at 37°C for 18–24 h. *H. bluephagenesis* was plated onto LB agar
593 supplemented with 6 × NaCl (60 g L^{-1} NaCl), *S. aureus* onto MH agar, and *S. cerevisiae*

594 onto YPD or YPEG agar at 30°C. CFUs were enumerated, and the bactericidal rate was
595 calculated as: Bactericidal rate (%) = $(1 - CFU_{sample} / CFU_{control}) \times 100$. The MBC was
596 defined as the lowest peptide concentration resulting in ≥ 99.9% reduction in CFUs
597 compared to the untreated control (corresponding to ≤ 0.1% survival). All assays were
598 performed in triplicate.

599 **Cytotoxicity determination**

600 Cytotoxicity was evaluated using the Cell Counting Kit-8 (C6005; NCM Biotech).
601 HEK293T cells were cultured in Dulbecco's Modified Eagle Medium (DMEM)
602 supplemented with 10% fetal bovine serum (FBS) at 37°C in 5% CO_2 for 24 h. Cells
603 were then subcultured, diluted to 1×10^5 cells mL^{-1}, and 50 μL suspension was
604 transferred to each well of a 96-well microplate. After 24 h, DMEM containing different
605 concentrations of c_AMPs was dispensed to each well. Cells were treated with c_AMPs
606 for 48 h. Subsequently, 10 μL of CCK-8 solution was added to each well and incubated
607 for 30 min at 37°C, after which absorbance at 450 nm was measured using a microplate
608 reader. Relative cell viability was calculated as $(OD_{450\ sample} - OD_{450\ blank}) / (OD_{450\ control}$
609 $- OD_{450\ blank})$. All assays were performed with three biological replicates. The same
610 procedure was applied to HepG2 and HeLa cells.

611 **Transmission electron microscopy examination**

612 *P. filamentosa* cells were treated with three deep-sea c_AMPs (cold seep-32, cold seep-
613 37, and hydrothermal vent-19) at a final concentration of 1 × MIC. In contrast, the
614 control group received phosphate-buffered saline (PBS) under the same conditions.
615 After incubation at 37°C for 2 h following previous studies[105], bacterial suspensions
616 were collected by centrifugation (6,000 r.p.m, 1 min, 4°C) and washed twice with PBS.
617 Cell pellets were resuspended and immediately processed for ultrathin sectioning for
618 observation. Samples were mounted on copper grids, negatively stained with 1% (w/v)
619 uranyl acetate for 15 s, air-dried, and examined using a transmission electron
620 microscope (TEM; Thermo Fisher Scientific Helios 5 UC) operated at 80 kV.

621 Morphological alterations in cell walls and membranes were compared between
622 peptide-treated and control cells.

623 **RNA sequencing and analysis**

624 To investigate transcriptional responses induced by representative c_AMPs, *P.*
625 *filamentosa* was treated with hydrothermal vent-19 (1 × MIC), *V. parahaemolyticus*
626 with hydrothermal vent-19 (1 × MIC), *A. pittii* with cold seep-9 (1 × MIC), and *S.*
627 *cerevisiae* with cold seep-38 (1 × MIC) for 4 h, each with three biological replicates.
628 PBS was used as the control. Total RNA was extracted using TRIzol® reagent
629 (Invitrogen) following the manufacturer's instructions and treated with DNase I
630 (TaKaRa) to remove residual genomic DNA. RNA integrity and purity were assessed
631 using an Agilent 2100 Bioanalyzer (Agilent Technologies) and a NanoDrop ND-2000
632 spectrophotometer (Thermo Fisher Scientific). High-quality RNA samples ($OD_{260/280}$ =
633 1.8–2.2, $OD_{260/230} \geq 2.0$, RIN ≥ 6.5, 28S:18S ≥ 1.0, and total RNA ≥ 10 μg) were used
634 for library construction.

635 For prokaryotic samples, rRNA was removed using the Ribo-Zero rRNA Removal Kit
636 (Epicenter), and strand-specific libraries were constructed from 5 μg of total RNA
637 following standard protocols. RNA was fragmented, reverse-transcribed into cDNA,
638 end-repaired, adenylated, and ligated to indexed adaptors. Libraries were size-selected
639 for 200–300 bp cDNA fragments using 2% Low Range Ultra Agarose and PCR-
640 amplified with Phusion DNA polymerase (NEB). For the eukaryotic sample (*S.*
641 *cerevisiae*), poly (A) + mRNA was purified using oligo (dT) magnetic beads,
642 fragmented, and processed using the same workflow. Final libraries were quantified
643 using a TBS380 fluorometer (Turner Biosystems) and sequenced on the MGI-T7
644 DNBSEQ platform (Shanghai BIOZERON Biotech) with 150 bp paired-end reads.

645 Raw reads were processed using Trimmomatic[106] (v0.36; parameters:
646 SLIDINGWINDOW:4:15 MINLEN:75) to remove adaptors, low-quality bases, and
647 short reads. Reads containing more than 10% ambiguous bases (N) were discarded.

648 Quality-controlled reads were further filtered against the rRNA database[107] (Rfam)
649 using sortmeRNA[108] (v2.1) to remove rRNA contaminants. For bacterial samples, clean
650 reads were aligned to the respective reference genomes using Rockhopper[109]. For *S.*
651 *cerevisiae*, reads were aligned to the reference genome using HISAT2 [110], and gene-
652 level counts were obtained using featureCounts (http://subread.sourceforge.net/). Gene
653 expression levels were normalized as reads per kilobase of transcript per million
654 mapped reads (RPKM)[111]. Differential expression and functional enrichment analyses
655 were performed on the CFViSA[112] platform. DEGs between treatment and control
656 groups were identified using edgeR[113] with thresholds of $|\log_2(\text{fold change})| \geq 1$ and
657 false discovery rate (FDR) < 0.05. GO enrichment analysis was performed using
658 Goatools[114], and KEGG pathway enrichment was conducted using KOBAS[115]. GO
659 terms[116] and KEGGpathways[117] with Bonferroni-corrected $P < 0.05$ were considered
660 significantly enriched.

661 **Statistical analysis**

662 Statistical analyses were performed using R v4.2.3. Data normality was assessed using
663 the Shapiro–Wilk test prior to downstream analyses. The Kruskal–Wallis rank-sum test
664 was used to compare physicochemical properties across deep-sea c_AMPs and
665 reference AMP datasets. Pairwise comparisons were conducted using Wilcoxon rank-
666 sum tests, and *P* values were adjusted using the Bonferroni correction. Corrected $P <$
667 0.05 was considered statistically significant.

668 **Data availability**

669 All transcriptome sequencing data generated in this study have been deposited in
670 Genome Sequence Archive (GSA) under accession number PRJCA052490. Sequence
671 files for smORF and c_AMP datasets from the five deep-sea habitats have been
672 deposited on Figshare (DOI: 10.6084/m9.figshare.30692342).

Code availability

Original codes have been deposited at Figshare (DOI: 10.6084/m9.figshare.30692342). All computational tools used in this study were executed with default parameters unless otherwise specified, as detailed in the Methods.

References

1. Zhang, C., Peng, Y., Liu, X., Wang, J. & Dong, X. Deep-sea microbial genetic resources: new frontiers for bioprospecting. *Trends in Microbiology* **32**, 321-324 (2024).
2. Wright, E.S. & Vetsigian, K.H. Inhibitory interactions promote frequent bistability among competing bacteria. *Nature Communications* **7**, 11274 (2016).
3. Dong, X. et al. A vast repertoire of secondary metabolites potentially influences community dynamics and biogeochemical processes in cold seeps. *Science Advances* **10**, eadl2281 (2024).
4. Duan, Y. et al. A catalog of small proteins from the global microbiome. *Nature Communications* **15**, 7563 (2024).
5. Storz, G., Wolf, Y.I. & Ramamurthi, K.S. Small proteins can no longer be ignored. *Annual Review of Biochemistry* **83**, 753-777 (2014).
6. Gaßel, M., Möllenkamp, T., Puppe, W. & Altendorf, K. The KdpF subunit is part of the K^+-translocating Kdp complex of *Escherichia coli* and is responsible for stabilization of the complex *in vitro*. *Journal of Biological Chemistry* **274**, 37901-37907 (1999).
7. Salazar, M.E., Podgornaia, A.I. & Laub, M.T. The small membrane protein MgrB regulates PhoQ bifunctionality to control PhoP target gene expression dynamics. *Molecular Microbiology* **102**, 430-445 (2016).
8. Lloyd, C.R., Park, S., Fei, J. & Vanderpool, C.K. The small protein SgrT controls transport activity of the glucose-specific phosphotransferase system. *Journal of Bacteriology* **199**, 10.1128/jb. 00869-00816 (2017).
9. Alix, E. & Blanc-Potard, A.B. Hydrophobic peptides: novel regulators within bacterial membrane. *Molecular Microbiology* **72**, 5-11 (2009).
10. Sassone-Corsi, M. et al. Microcins mediate competition among *Enterobacteriaceae* in the inflamed gut. *Nature* **540**, 280-283 (2016).
11. Lazzaro, B.P., Zasloff, M. & Rolff, J. Antimicrobial peptides: Application informed by evolution. *Science* **368**, eaau5480 (2020).
12. Yu, G., Baeder, D.Y., Regoes, R.R. & Rolff, J. Predicting drug resistance evolution: insights from antimicrobial peptides and antibiotics. *Proceedings of the Royal Society B: Biological Sciences* **285**, 20172687 (2018).
13. Kintses, B. et al. Phylogenetic barriers to horizontal transfer of antimicrobial peptide resistance genes in the human gut microbiota. *Nature Microbiology* **4**, 447-458 (2019).
14. Ahrens, C.H., Wade, J.T., Champion, M.M. & Langer, J.D. A practical guide to small protein discovery and characterization using mass spectrometry. *Journal of Bacteriology* **204**, e00353-00321 (2022).

15. Hyatt, D. et al. Prodigal: prokaryotic gene recognition and translation initiation site identification. *BMC Bioinformatics* **11**, 1-11 (2010).
16. Aspden, J.L. et al. Extensive translation of small open reading frames revealed by Poly-Ribo-Seq. *eLife* **3**, e03528 (2014).
17. Leong, A.Z.-X. et al. Short open reading frames (sORFs) and microproteins: an update on their identification and validation measures. *Journal of Biomedical Science* **29**, 19 (2022).
18. Rodríguez del Río, Á. et al. Functional and evolutionary significance of unknown genes from uncultivated taxa. *Nature* **626**, 377-384 (2024).
19. Ma, Y. et al. Identification of antimicrobial peptides from the human gut microbiome using deep learning. *Nature Biotechnology* **40**, 921-931 (2022).
20. Santos-Júnior, C.D. et al. Discovery of antimicrobial peptides in the global microbiome with machine learning. *Cell* **187**, 3761-3778.e3716 (2024).
21. Fan, S. et al. Bioprospecting of culturable marine biofilm bacteria for novel antimicrobial peptides. *iMeta* **3** (2024).
22. Han, Y. et al. A comprehensive genomic catalog from global cold seeps. *Scientific Data* **10**, 596 (2023).
23. Zhang, C. et al. The majority of microorganisms in gas hydrate-bearing subseafloor sediments ferment macromolecules. *Microbiome* **11**, 37 (2023).
24. Liang, X., Nong, X.-H., Huang, Z.-H. & Qi, S.-H. Antifungal and antiviral cyclic peptides from the deep-sea-derived fungus *Simplicillium obclavatum* EIODSF 020. *Journal of Agricultural and Food Chemistry* **65**, 5114-5121 (2017).
25. Zhou, X. et al. Marthiapeptide A, an anti-infective and cytotoxic polythiazole cyclopeptide from a 60 L scale fermentation of the deep sea-derived *Marinactinospora thermotolerans* SCSIO 00652. *Journal of Natural Products* **75**, 2251-2255 (2012).
26. Casella, V. et al. Novel insights into the *Nobilamide* family from a deep-sea *Bacillus*: Chemical diversity, biosynthesis and antimicrobial activity towards multidrug-resistant bacteria. *Marine Drugs* **23**, 41 (2025).
27. Lai, C. et al. New polyketides from a hydrothermal vent sediment fungus *Trichoderma* sp. JWM29-10-1 and their antimicrobial effects. *Marine Drugs* **20**, 720 (2022).
28. Wei, X., Hu, Y., Sun, C. & Wu, S. Characterization of a novel antimicrobial peptide bacipeptin against foodborne pathogens. *Journal of Agricultural and Food Chemistry* **72**, 5283-5292 (2024).
29. Hancock, R.E.W. & Lehrer, R. Cationic peptides: a new source of antibiotics. *Trends in Biotechnology* **16**, 82-88 (1998).
30. Koehbach, J. & Craik, D.J. The vast structural diversity of antimicrobial peptides. *Trends in Pharmacological Sciences* **40**, 517-528 (2019).
31. Oliveira Junior, N.G., Souza, C.M., Buccini, D.F., Cardoso, M.H. & Franco, O.L. Antimicrobial peptides: structure, functions and translational applications. *Nature Reviews Microbiology* **23**, 687–700 (2025).
32. Sneideris, T. et al. Targeting nucleic acid phase transitions as a mechanism of action for antimicrobial peptides. *Nature Communications* **14**, 7170 (2023).
33. Seefeldt, A.C. et al. Structure of the mammalian antimicrobial peptide Bac7(1–16) bound within the exit tunnel of a bacterial ribosome. *Nucleic Acids Research* **44**, 2429-2438 (2016).
34. Ghosh, A. et al. Indolicidin targets duplex DNA: structural and mechanistic insight through a

755 combination of spectroscopy and microscopy. *ChemMedChem* **9**, 2052-2058 (2014).
756 35. Hahnfeld, J.M. et al. sORFdb–a database for sORFs, small proteins, and small protein families
757 in bacteria. *BMC Genomics* **26**, 110 (2025).
758 36. Li, Y. et al. SmProt: A reliable repository with comprehensive annotation of small proteins
759 identified from ribosome profiling. *Genomics, Proteomics & Bioinformatics* **19**, 602-610 (2021).
760 37. Xiao, X. et al. Microbial ecosystems and ecological driving forces in the deepest ocean
761 sediments. *Cell* **188**, 1363-1377.e1369 (2025).
762 38. Dick, G.J. The microbiomes of deep-sea hydrothermal vents: distributed globally, shaped locally.
763 *Nature Reviews Microbiology* **17**, 271-283 (2019).
764 39. Orcutt, B.N., Sylvan, J.B., Knab, N.J. & Edwards, K.J. Microbial ecology of the dark ocean
765 above, at, and below the seafloor. *Microbiol Mol Biol Rev* **75**, 361-422 (2011).
766 40. Nunoura, T. et al. Microbial diversity in sediments from the bottom of the Challenger Deep, the
767 Mariana Trench. *Microbes and Environments* **33**, 186-194 (2018).
768 41. Schauberger, C. et al. Microbial community structure in hadal sediments: high similarity along
769 trench axes and strong changes along redox gradients. *The ISME Journal* **15**, 3455-3467 (2021).
770 42. Jiao, Y., Yang, S. & Bao, W. Biogeographic patterns and community assembly mechanisms of
771 bacterial community in the upper seawater of seamounts and non-seamounts in the Eastern
772 Indian Ocean. *Applied and Environmental Microbiology* **90**, e01424-01424 (2024).
773 43. Li, H., Zhou, H., Yang, S. & Dai, X. Stochastic and deterministic assembly processes in
774 seamount microbial communities. *Applied and Environmental Microbiology* **89**, e00701-00723
775 (2023).
776 44. Mirdita, M., Steinegger, M., Breitwieser, F., Söding, J. & Levy Karin, E. Fast and sensitive
777 taxonomic assignment to metagenomic contigs. *Bioinformatics* **37**, 3029-3031 (2021).
778 45. Parks, D.H. et al. GTDB: an ongoing census of bacterial and archaeal diversity through a
779 phylogenetically consistent, rank normalized and complete genome-based taxonomy. *Nucleic*
780 *Acids Research* **50**, D785-D794 (2022).
781 46. Li, Y., Cao, W., Wang, Y. & Ma, Q. Microbial diversity in the sediments of the southern Mariana
782 Trench. *Journal of Oceanology and Limnology* **37**, 1024-1029 (2019).
783 47. Tully, B.J., Graham, E.D. & Heidelberg, J.F. The reconstruction of 2,631 draft metagenome-
784 assembled genomes from the global oceans. *Scientific Data* **5**, 170203 (2018).
785 48. Zhou, Y.-L., Mara, P., Cui, G.-J., Edgcomb, V.P. & Wang, Y. Microbiomes in the Challenger
786 Deep slope and bottom-axis sediments. *Nature Communications* **13**, 1515 (2022).
787 49. Jiang, Q. et al. Cold seeps are potential hotspots of deep-sea nitrogen loss driven by
788 microorganisms across 21 phyla. *Nature Communications* **16**, 1646 (2025).
789 50. Galperin, M.Y. et al. COG database update: focus on microbial diversity, model organisms, and
790 widespread pathogens. *Nucleic Acids Research* **49**, D274-D281 (2021).
791 51. Miravet-Verde, S. et al. Unraveling the hidden universe of small proteins in bacterial genomes.
792 *Molecular Systems Biology* **15**, e8290 (2019).
793 52. Yadavalli, S.S. & Yuan, J. Bacterial small membrane proteins: the swiss army knife of regulators
794 at the lipid bilayer. *Journal of Bacteriology* **204**, e00344-00321 (2022).
795 53. Ma, T. et al. DRAMP 4.0: an open-access data repository dedicated to the clinical translation of
796 antimicrobial peptides. *Nucleic Acids Research* **53**, D403-D410 (2024).
797 54. Wang, G., Li, X. & Wang, Z. APD3: the antimicrobial peptide database as a tool for research
798 and education. *Nucleic Acids Research* **44**, D1087-D1093 (2015).

55. Torres, M.D.T. et al. Mining for encrypted peptide antibiotics in the human proteome. *Nature Biomedical Engineering* **6**, 67-75 (2022).
56. Le, C.-F., Fang, C.-M. & Sekaran, S.D. Intracellular targeting mechanisms by antimicrobial peptides. *Antimicrobial Agents and Chemotherapy* **61**, 10.1128/aac.02340-02316 (2017).
57. Zhang, Q.-Y. et al. Antimicrobial peptides: mechanism of action, activity and clinical potential. *Military Medical Research* **8**, 48 (2021).
58. Melino, S. et al. Metal-binding and nuclease activity of an antimicrobial peptide analogue of the salivary histatin 5. *Biochemistry* **45**, 15373-15383 (2006).
59. Migliolo, L. et al. Structural and functional characterization of a multifunctional alanine-rich peptide analogue from *Pleuronectes americanus*. *PLOS ONE* **7**, e47047 (2012).
60. Yacoub, H.A., Al-Maghrabi, O.A., Ahmed, E.S. & Uversky, V.N. Abundance and functional roles of intrinsic disorder in the antimicrobial peptides of the NK-lysin family. *Journal of Biomolecular Structure and Dynamics* **35**, 836-856 (2017).
61. Balleza, D. The role of flexibility in the bioactivity of short *α*-helical antimicrobial peptides. *Antibiotics* **14**, 422 (2025).
62. Tuerkova, A. et al. Effect of helical kink in antimicrobial peptides on membrane pore formation. *eLife* **9**, e47946 (2020).
63. Cotter, P.D., Ross, R.P. & Hill, C. Bacteriocins—a viable alternative to antibiotics? *Nature Reviews Microbiology* **11**, 95-105 (2013).
64. Reddy, K.V.R., Yedery, R.D. & Aranha, C. Antimicrobial peptides: premises and promises. *International Journal of Antimicrobial Agents* **24**, 536-547 (2004).
65. Bass, D. et al. Yeast forms dominate fungal diversity in the deep oceans. *Proceedings of the Royal Society B: Biological Sciences* **274**, 3069-3077 (2007).
66. Yang, S., Xu, W., Gao, Y., Chen, X. & Luo, Z.-H. Fungal diversity in deep-sea sediments from Magellan seamounts environment of the western Pacific revealed by high-throughput Illumina sequencing. *Journal of Microbiology* **58**, 841-852 (2020).
67. Gaser, O.A. et al. Alteration of metabolic activity regulates mitochondrial temperature in diagnosis in HepG2 hepatocellular carcinoma cells. *Scientific Reports* **15**, 41155 (2025).
68. Hancock, R.E.W. & Sahl, H.-G. Antimicrobial and host-defense peptides as new anti-infective therapeutic strategies. *Nature Biotechnology* **24**, 1551-1557 (2006).
69. Zhong, C. et al. An antimicrobial peptide as a potential therapy for bacterial pneumonia that alleviates antimicrobial resistance. *Nature Communications* **16**, 10488 (2025).
70. Giacomucci, S., Cros, C.D.-N., Perron, X., Mathieu-Denoncourt, A. & Duperthuy, M. Flagella-dependent inhibition of biofilm formation by sub-inhibitory concentration of polymyxin B in Vibrio cholerae. *PLOS ONE* **14**, e0221431 (2019).
71. Plaza, N., Pérez-Reytor, D., Corsini, G., García, K. & Urrutia, Í.M. Contribution of the type III secretion system (T3SS2) of *Vibrio parahaemolyticus* in mitochondrial stress in human intestinal cells. *Microorganisms* **12**, 813 (2024).
72. Antonietti, M. et al. An analysis of intrinsic protein disorder in antimicrobial peptides. *The Protein Journal* **44**, 175-191 (2025).
73. Busch, D.J. et al. Intrinsically disordered proteins drive membrane curvature. *Nature Communications* **6**, 7875 (2015).
74. Gong, H. et al. How do antimicrobial peptides disrupt the lipopolysaccharide membrane leaflet of Gram-negative bacteria? *Journal of Colloid and Interface Science* **637**, 182-192 (2023).

75. Li, J. et al. Deep sea cold seeps are a sink for mercury and source for methylmercury. *Communications Earth & Environment* **5**, 324 (2024).
76. Dong, X. et al. Metabolic potential of uncultured bacteria and archaea associated with petroleum seepage in deep-sea sediments. *Nature Communications* **10**, 1816 (2019).
77. Dong, X. et al. Phylogenetically and catabolically diverse diazotrophs reside in deep-sea cold seep sediments. *Nature Communications* **13**, 4885 (2022).
78. Dong, X. et al. Thermogenic hydrocarbon biodegradation by diverse depth-stratified microbial populations at a Scotian Basin cold seep. *Nature Communications* **11**, 5825 (2020).
79. Jiang, Q., Jing, H., Jiang, Q. & Zhang, Y. Insights into carbon-fixation pathways through metagonomics in the sediments of deep-sea cold seeps. *Marine Pollution Bulletin* **176**, 113458 (2022).
80. Lu, R. et al. Asgard archaea in the haima cold seep: Spatial distribution and genomic insights. *Deep Sea Research Part I: Oceanographic Research Papers* **170**, 103489 (2021).
81. Li, W.-L., Wu, Y.-Z., Zhou, G.-w., Huang, H. & Wang, Y. Metabolic diversification of anaerobic methanotrophic archaea in a deep-sea cold seep. *Marine Life Science & Technology* **2**, 431-441 (2020).
82. Xiao, X. et al. Metal-driven anaerobic oxidation of methane as an important methane sink in methanic cold seep sediments. *Microbiology Spectrum* **11**, e05337-05322 (2023).
83. Chen, S., Zhou, Y., Chen, Y. & Gu, J. fastp: an ultra-fast all-in-one FASTQ preprocessor. *Bioinformatics* **34**, i884-i890 (2018).
84. Li, D., Liu, C.-M., Luo, R., Sadakane, K. & Lam, T.-W. MEGAHIT: an ultra-fast single-node solution for large and complex metagenomics assembly via succinct de Bruijn graph. *Bioinformatics* **31**, 1674-1676 (2015).
85. Durrant, M.G. & Bhatt, A.S. Automated prediction and annotation of small open reading frames in microbial genomes. *Cell Host & Microbe* **29**, 121-131.e124 (2021).
86. Fu, L., Niu, B., Zhu, Z., Wu, S. & Li, W. CD-HIT: accelerated for clustering the next-generation sequencing data. *Bioinformatics* **28**, 3150-3152 (2012).
87. Steinegger, M. & Söding, J. MMseqs2 enables sensitive protein sequence searching for the analysis of massive data sets. *Nature Biotechnology* **35**, 1026-1028 (2017).
88. Buchfink, B., Reuter, K. & Drost, H.G. Sensitive protein alignments at tree-of-life scale using DIAMOND. *Nature Methods* **18**, 366-368 (2021).
89. Cantalapiedra, C.P., Hernández-Plaza, A., Letunic, I., Bork, P. & Huerta-Cepas, J. eggNOG-mapper v2: functional annotation, orthology assignments, and domain prediction at the metagenomic scale. *Molecular Biology and Evolution* **38**, 5825-5829 (2021).
90. Huerta-Cepas, J. et al. eggNOG 5.0: a hierarchical, functionally and phylogenetically annotated orthology resource based on 5090 organisms and 2502 viruses. *Nucleic Acids Research* **47**, D309-D314 (2019).
91. Teufel, F. et al. SignalP 6.0 predicts all five types of signal peptides using protein language models. *Nature Biotechnology* **40**, 1023-1025 (2022).
92. Krogh, A., Larsson, B., von Heijne, G. & Sonnhammer, E.L.L. Predicting transmembrane protein topology with a hidden markov model: application to complete genomes11Edited by F. Cohen. *Journal of Molecular Biology* **305**, 567-580 (2001).
93. Santos-Junior, C.D., Pan, S., Zhao, X.-M. & Coelho, L.P. Macrel: antimicrobial peptide screening in genomes and metagenomes. *PeerJ* **8**, e10555 (2020).

94. Lawrence, T.J. et al. amPEPpy 1.0: a portable and accurate antimicrobial peptide prediction tool. *Bioinformatics* **37**, 2058-2060 (2020).
95. Li, C. et al. AMPlify: attentive deep learning model for discovery of novel antimicrobial peptides effective against WHO priority pathogens. *BMC Genomics* **23**, 77 (2022).
96. Jumper, J. et al. Highly accurate protein structure prediction with AlphaFold. *Nature* **596**, 583-589 (2021).
97. Abramson, J. et al. Accurate structure prediction of biomolecular interactions with AlphaFold 3. *Nature* **630**, 493-500 (2024).
98. Kochendoerfer, G.G. & Kent, S.B.H. Chemical protein synthesis. *Current Opinion in Chemical Biology* **3**, 665-671 (1999).
99. Palomo, J.M. Solid-phase peptide synthesis: an overview focused on the preparation of biologically relevant peptides. *RSC Advances* **4**, 32658-32672 (2014).
100. Wang, B. et al. Explainable deep learning and virtual evolution identifies antimicrobial peptides with activity against multidrug-resistant human pathogens. *Nature Microbiology* **10**, 332-347 (2025).
101. O'Shea, K. & Nash, R. An introduction to convolutional neural networks. *ArXiv* Preprint at https://arxiv.org/abs/1511.08458 (2015).
102. Hochreiter, S. & Schmidhuber, J. Long short-term memory. *Neural Computation* **9**, 1735–1780 (1997).
103. Vaswani, A. et al. in Proceedings of the 31st International Conference on Neural Information Processing Systems 6000–6010 (Curran Associates Inc., Long Beach, California, USA; 2017).
104. Hebditch, M., Carballo-Amador, M.A., Charonis, S., Curtis, R. & Warwicker, J. Protein–Sol: a web tool for predicting protein solubility from sequence. *Bioinformatics* **33**, 3098-3100 (2017).
105. Wang, T. et al. The effect of structural modification of antimicrobial peptides on their antimicrobial activity, hemolytic activity, and plasma stability. *Journal of Peptide Science* **27**, e3306 (2021).
106. Bolger, A.M., Lohse, M. & Usadel, B. Trimmomatic: a flexible trimmer for Illumina sequence data. *Bioinformatics* **30**, 2114-2120 (2014).
107. Sellés Vidal, L., Ayala, R., Stan, G.-B. & Ledesma-Amaro, R. rfaRm: An R client-side interface to facilitate the analysis of the Rfam database of RNA families. *PLOS ONE* **16**, e0245280 (2021).
108. Kopylova, E., Noé, L. & Touzet, H. SortMeRNA: fast and accurate filtering of ribosomal RNAs in metatranscriptomic data. *Bioinformatics* **28**, 3211-3217 (2012).
109. Slezacek, J., Quillfeldt, P., Kaiya, H., Hykollari, A. & Fusani, L. Circulating profile of the appetite-regulating hormone ghrelin during moult-fast and chick provisioning in southern rockhopper penguins (*Eudyptes chrysocome chrysocome*). *Hormones and Behavior* **164**, 105592 (2024).
110. Thakur, V. Transcriptome Data Analysis. (Springer US, New York, NY; 2024).
111. Ke, Y. et al. The progressive application of single-cell RNA sequencing technology in cardiovascular diseases. *Biomedicine & Pharmacotherapy* **154**, 113604 (2022).
112. Wang, N. et al. CFViSA: A comprehensive and free platform for visualization and statistics in omics-data. *Computers in Biology and Medicine* **171**, 108206 (2024).
113. Sarker, B., Matiur Rahaman, M., Alamin, M.H., Ariful Islam, M. & Nurul Haque Mollah, M. Boosting edgeR (Robust) by dealing with missing observations and gene-specific outliers in RNA-Seq profiles and its application to explore biomarker genes for diagnosis and therapies of

ovarian cancer. *Genomics* **116**, 110834 (2024).
114. Klopfenstein, D.V. et al. GOATOOLS: A python library for gene ontology analyses. *Scientific Reports* **8**, 10872 (2018).
115. Bu, D. et al. KOBAS-i: intelligent prioritization and exploratory visualization of biological functions for gene enrichment analysis. *Nucleic Acids Research* **49**, W317-W325 (2021).
116. Yan, H., Wang, S., Liu, H., Mamitsuka, H. & Zhu, S. GORetriever: reranking protein-description-based GO candidates by literature-driven deep information retrieval for protein function annotation. *Bioinformatics* **40**, ii53-ii61 (2024).
117. Yaning, L. et al. Cpd861 targeting BCL2 to alleviate hepatic fibrosis: Network pharmacology, mendelian randomization, and molecular docking mechanisms. *Current Pharmaceutical Design* **30**, 3291-3310 (2024).

Acknowledgements

This work was supported by National Key R & D Program of China (2022YFC2805505, 2024YFA0916503); National Natural Science Foundation of China (42376115, 42406109, 32122050, 32370074); Natural Science Foundation of Fujian Province (2023J06042, 2025J011005); Scientific Research Foundation of Third Institute of Oceanography, MNR (2025013); and Hubei Hongshan Laboratory (CDSJ, 2025hsqd014). We thank Tianxueyu Zhang and Ruiqi Lin for assistance with data collection, Hai Zhang, Chen Ling, Xianming Deng for providing strains, and Qiang Zheng, Weipeng Zhang, Fabai Wu, and Rui Cheng for helpful discussions.

Author contributions

X.D. and Z.L. conceived and designed the study. Q.J. and Y.H. carried out the omics analyses. Z.L. and C.Y. performed the experiments. Y.D., F.L., Z.H. and C.S. contributed to methodological development and discussions. Q.J., Y.H., X.D. and Z.L. wrote the manuscript with input from all authors. All authors reviewed and approved the final manuscript.

Competing interests

The authors declare no competing interests.

Figure legends

Figure 1. A global atlas of deep-sea small proteins with unprecedented diversity and novelty. (a) Geographic distribution of the deep-sea sampling sites included in this study. Circles denote metagenomic sampling locations, and squares indicate the number of samples collected at each site. Sampling and sequencing metadata for all datasets are provided in **Supplementary Table 1**. The world map was generated using Ocean Data View (ODV 5.1.7). **(b)** Workflow for predicting smORFs and candidate antimicrobial peptides (c_AMPs). Details are provided in methods. **(c)** Comparative homology landscape showing the novelty of deep-sea smORFs relative to existing small-protein databases. For each habitat, the proportions of smORFs with detectable homologs versus novel smORFs lacking database matches are shown. Some smORFs map to multiple databases; therefore, counts are not additive across databases. Detailed homology statistics are reported in **Supplementary Table 2**. **(d)** Functional annotation of smORF catalogs from the five deep-sea habitats, based on KEGG, eggNOG, CAZy, and Pfam databases. Summary statistics provided in **Supplementary Table 2**.

Figure 2. Habitat-specific patterns of deep-sea smORFs. (a) Shared smORFs across the five deep-sea habitats. Ribbon widths represent the proportion of smORFs shared between habitats, with numerical labels indicating the percentage of each habitat's smORF catalog that is shared with others. Owing to the large disparities in smORF catalog sizes among habitats, truncated axes are used to improve visualization. Detailed pairwise comparisons are provided in **Supplementary Table 3**. **(b)** Functional annotation of shared small proteins based on the COG database. COG categories are grouped into four major functional classes. Colors correspond to individual COG categories within these groups. **(c)** Taxonomic annotation of smORFs across the five habitats. Stacked bar charts show the relative abundance of archaeal and bacterial taxa at class level. Taxonomic assignment was performed using GTDB release R220. Detailed habitat-specific taxonomic profiles are provided in **Supplementary Tables 6–7**. **(d)** Proportions of smORF-derived proteins predicted to contain transmembrane

988 domains or signal peptides across habitats. Values shown in the radial plots indicate the
989 percentage of small proteins carrying the corresponding structural feature in each
990 habitat. Detailed information is provided in **Supplementary Table 9**.

991 **Figure 3. Defining a new structural and biophysical class of deep-sea antimicrobial**
992 **peptides (c_AMPs). (a)** Novelty assessment of c_AMPs identified across the five
993 deep-sea habitats, benchmarked against experimentally validated AMP databases and
994 large-scale predicted AMP resources. Bubble plots summarize the proportion of
995 homologous (light color) versus novel sequences (dark color). **(b)** Normalized amino-
996 acid composition profiles of deep-sea c_AMPs compared with reference AMP datasets.
997 Detailed information is provided in **Supplementary Table 10**. **(c)** Multidimensional
998 comparison of physicochemical descriptors across habitats and reference datasets.
999 Detailed physicochemical properties and statistical data are provided in
1000 **Supplementary Tables 10-12. (d)** Representative AlphaFold2-predicted structures
1001 illustrating the conformational diversity of c_AMPs from different habitats. Model
1002 confidence is reported as per-residue pLDDT scores, highlighting ordered secondary-
1003 structure elements (α-helices, β-sheets) alongside flexible or disordered regions.

1004 **Figure 4. Functional validation of representative deep-sea c_AMPs. (a)** Broad-
1005 spectrum inhibitory activity of synthetic c_AMPs against four non-pathogenic and five
1006 pathogenic microorganisms. MICs were determined using two-fold serial dilutions
1007 (2.5–125 μM) in 96-well plates containing ~1×10^5 CFU/mL. MIC values represent the
1008 mean concentration across three independent dilution series. Gram-positive (+) and
1009 Gram-negative (−) species are indicated. Detail information on MICs is provided in
1010 **Supplementary Tables 14-15**. **(b)** Bactericidal activity of representative c_AMPs at
1011 1× MIC against *P. filamentosa*, *H. bluephagenesis*, *V. parahaemolyticus*, *A. pittii*, and
1012 *E. coli* DH5α. The minimum bactericidal concentration (MBC) was defined as the
1013 lowest concentration yielding ≥ 99.9% killing (≤ 0.1% survival). Representative plate
1014 images are shown. All assays were performed in triplicate. Detail information on MBCs
1015 is provided in **Supplementary Table 16**. **(c)** Cytotoxicity of synthetic c_AMPs toward

1016 mammalian cells (HEK293T, HepG2, HeLa) at 1–2 × MIC, assessed using standard
1017 metabolic-activity assays. Data represent mean ± SD from independent experiments.
1018 Detail data are provided in **Supplementary Table 17**.

1019 **Figure 5. Mechanistic insights into deep-sea c_AMP activity across multiple**
1020 **microorganisms. (a)** Diamond plots showing differentially expressed genes (DEGs) in
1021 four microorganisms treated with representative c_AMPs. Numbers within each sector
1022 indicate total DEGs, with light and dark colors marking significantly up- and
1023 downregulated genes, respectively. Detailed lists of up- and down-regulated genes for
1024 each treatment group are presented in **Supplementary Tables 18–21**. **(b–c)** Proposed
1025 mechanism of action of cold seep-9 in *A. pittii*, including GO enrichment analysis of
1026 DEGs ($P < 0.05$) (b) and a structural model of an ABC transporter permease subunit
1027 (light blue/gray) bound to cold seep-9 (green) (c). Protein–peptide complexes were
1028 generated using AlphaFold3, and model quality was assessed using ipTM and pTM
1029 scores. Insets highlight predicted interaction interfaces between the peptide and the
1030 permease. **(d–f)** Proposed mechanism of action of hydrothermal vent-19 in *P.*
1031 *filamentosa*, including KEGG KO enrichment analysis of DEGs (d), GO enrichment
1032 analysis ($P < 0.005$) (e), and an AlphaFold-based structural model of tRNA
1033 pseudouridine synthase TruA (light blue) bound to hydrothermal vent-19 (green) (f),
1034 with predicted peptide–protein interaction residues indicated. **(g)** Transmission electron
1035 microscopy (TEM) images of *P. filamentosa* treated with hydrothermal vent-19, cold
1036 seep-32, and cold seep-37 at 1× MIC. All TEM experiments were performed in
1037 triplicate. Scale bars: 10 μm. **(h–i)** Proposed mechanism of action of hydrothermal vent-
1038 19 in *V. parahaemolyticus*, including KEGG KO enrichment analysis showing
1039 significantly enriched pathways (h) and a structural model of tRNA 2-thiocytidine (32)
1040 synthetase (TtcA; light blue) bound to hydrothermal vent-19 (green), highlighting
1041 predicted interaction residues (i). All structural models were visualized using PyMOL.

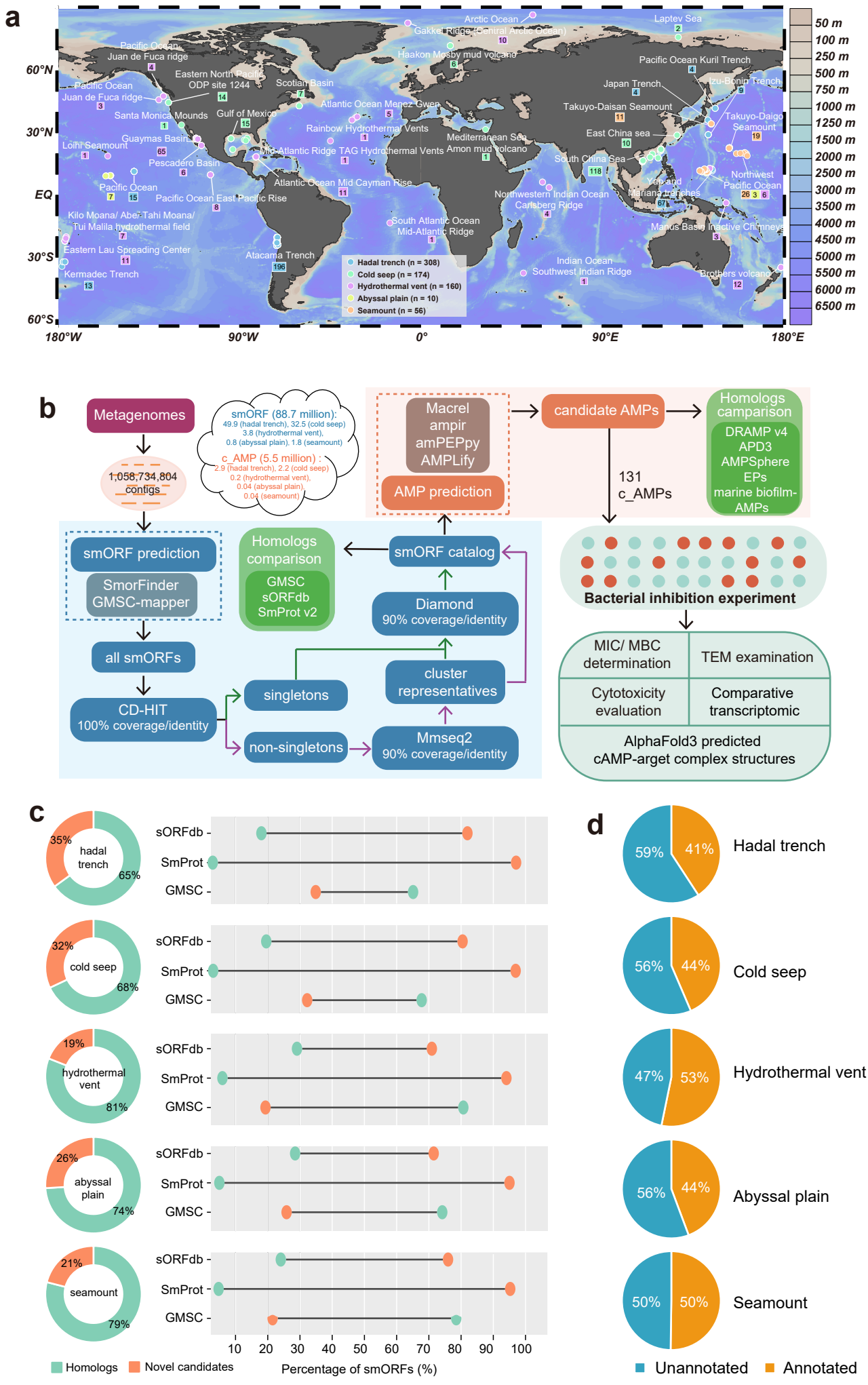
a
Arctic Ocean
Gakkel Ridge (Central Arctic Ocean)
Laptev Sea
Pacific Ocean
Juan de Fuca ridge
Haakon Mosby mud volcano
Pacific Ocean Kuril Trench
Eastern North Pacific
ODP site 1244
Scotian Basin
Japan Trench
Izu-Bonin Trench
Pacific Ocean
Juan de Fuca ridge
Atlantic Ocean Menez Gwen
Takuyo-Daisan Seamount
Santa Monica Mounds
Gulf of Mexico
Rainbow Hydrothermal Vents
Takuyo-Daigo Seamount
Guaymas Basin
Mediterranean Sea
East China sea
Loihi Seamount
Mid-Atlantic Ridge TAG Hydrothermal Vents
Amon mud volcano
Pescadero Basin
South China Sea
Northwest Pacific Ocean
Pacific Ocean
Atlantic Ocean Mid Cayman Rise
Pacific Ocean East Pacific Rise
Northwestern Indian Ocean
Carlsberg Ridge
Yap and Mariana trenches
Kilo Moana/ Abe/ Tahi Moana/
Tui Malila hydrothermal field
South Atlantic Ocean
Mid-Atlantic Ridge
Manus Basin Inactive Chimney
Eastern Lau Spreading Center
Atacama Trench
Kermadec Trench
Indian Ocean
Southwest Indian Ridge
Brothers volcano
Hadal trench (n = 308)
Cold seep (n = 174)
Hydrothermal vent (n = 160)
Abyssal plain (n = 10)
Seamount (n = 56)
60°N
30°N
EQ
30°S
60°S
180°W
90°W
0°
90°E
180°E
50 m
100 m
250 m
500 m
750 m
1000 m
1250 m
1500 m
2000 m
2500 m
3000 m
3500 m
4000 m
4500 m
5000 m
5500 m
6000 m
6500 m
b
Metagenomes
1,058,734,804 contigs
smORF (88.7 million):
49.9 (hadal trench), 32.5 (cold seep)
3.8 (hydrothermal vent),
0.8 (abyssal plain), 1.8 (seamount)
c_AMP (5.5 million) :
2.9 (hadal trench), 2.2 (cold seep)
0.2 (hydrothermal vent),
0.04 (abyssal plain),
0.04 (seamount)
Macrel
ampir
amPEPpy
AMPLify
AMP prediction
candidate AMPs
Homologs camparison
DRAMP v4
APD3
AMPSphere
EPs
marine biofilm-AMPs
131 c_AMPs
smORF prediction
SmorFinder
GMSC-mapper
Homologs comparison
GMSC
sORFdb
SmProt v2
smORF catalog
Diamond
90% coverage/identity
Bacterial inhibition experiment
all smORFs
cluster representatives
MIC/ MBC determination
TEM examination
CD-HIT
100% coverage/identity
singletons
non-singletons
Mmseq2
90% coverage/identity
Cytotoxicity evaluation
Comparative transcriptomic
AlphaFold3 predicted cAMP-arget complex structures
c
hadal trench
35%
65%
cold seep
32%
68%
hydrothermal vent
19%
81%
abyssal plain
26%
74%
seamount
21%
79%
sORFdb
SmProt
GMSC
10
20
30
40
50
60
70
80
90
100
Homologs
Novel candidates
Percentage of smORFs (%)
d
Hadal trench
59%
41%
Cold seep
56%
44%
Hydrothermal vent
47%
53%
Abyssal plain
56%
44%
Seamount
50%
50%
Unannotated
Annotated

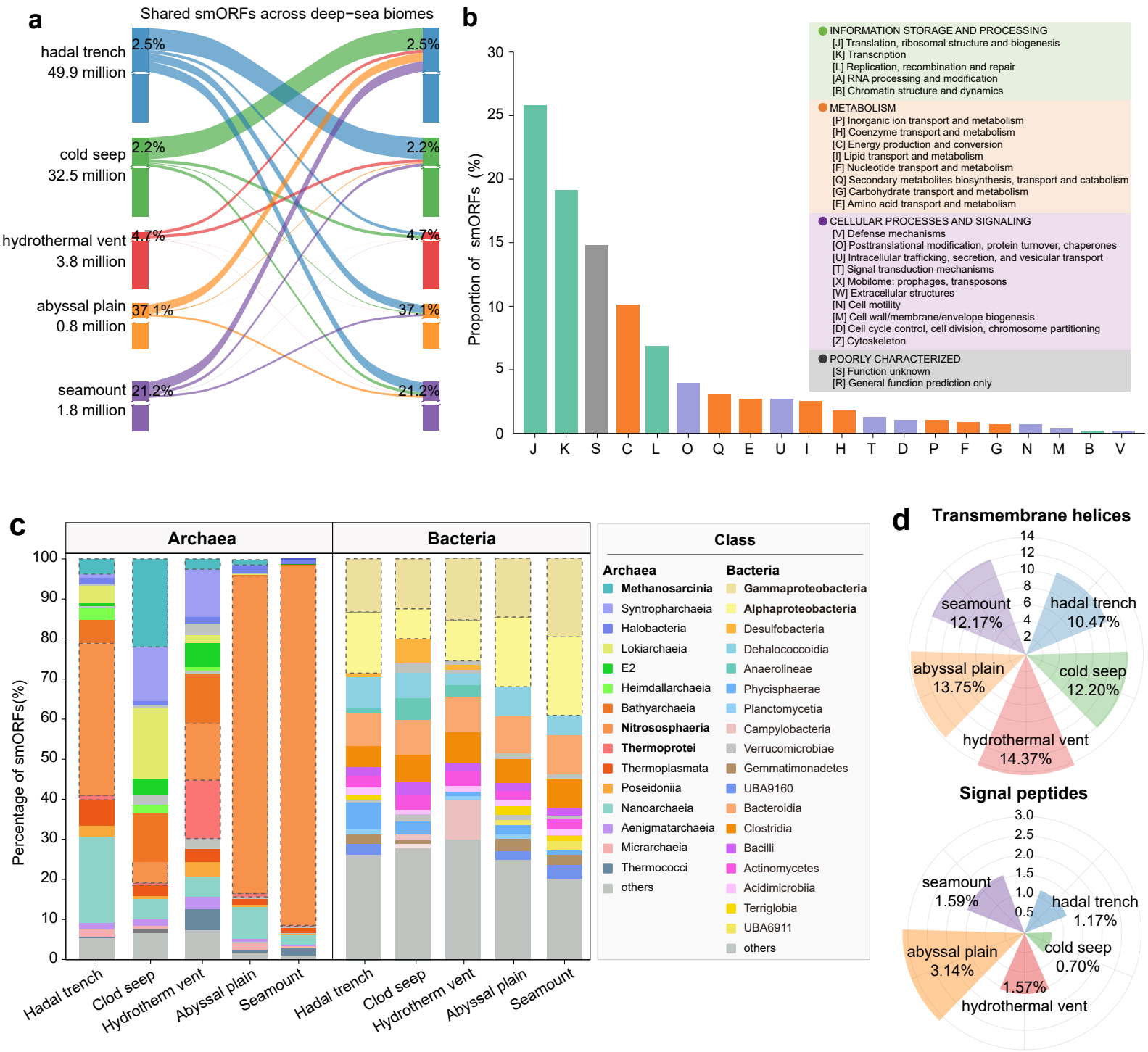
a
Shared smORFs across deep−sea biomes
hadal trench
49.9 million
cold seep
32.5 million
hydrothermal vent
3.8 million
abyssal plain
0.8 million
seamount
1.8 million
2.5%
2.2%
4.7%
37.1%
21.2%
b
Proportion of smORFs (%)
J K S C L O Q E U I H T D P F G N M B V
INFORMATION STORAGE AND PROCESSING
[J] Translation, ribosomal structure and biogenesis
[K] Transcription
[L] Replication, recombination and repair
[A] RNA processing and modification
[B] Chromatin structure and dynamics
METABOLISM
[P] Inorganic ion transport and metabolism
[H] Coenzyme transport and metabolism
[C] Energy production and conversion
[I] Lipid transport and metabolism
[F] Nucleotide transport and metabolism
[Q] Secondary metabolites biosynthesis, transport and catabolism
[G] Carbohydrate transport and metabolism
[E] Amino acid transport and metabolism
CELLULAR PROCESSES AND SIGNALING
[V] Defense mechanisms
[O] Posttranslational modification, protein turnover, chaperones
[U] Intracellular trafficking, secretion, and vesicular transport
[T] Signal transduction mechanisms
[X] Mobilome: prophages, transposons
[W] Extracellular structures
[N] Cell motility
[M] Cell wall/membrane/envelope biogenesis
[D] Cell cycle control, cell division, chromosome partitioning
[Z] Cytoskeleton
POORLY CHARACTERIZED
[S] Function unknown
[R] General function prediction only
c
Archaea
Bacteria
Percentage of smORFs(%)
Hadal trench
Clod seep
Hydrotherm vent
Abyssal plain
Seamount
Class
Archaea
Methanosarcinia
Syntropharchaeia
Halobacteria
Lokiarchaeia
E2
Heimdallarchaeia
Bathyarchaeia
Nitrososphaeria
Thermoprotei
Thermoplasmata
Poseidoniia
Nanoarchaeia
Aenigmatarchaeia
Micrarchaeia
Thermococci
others
Bacteria
Gammaproteobacteria
Alphaproteobacteria
Desulfobacteria
Dehalococcoidia
Anaerolineae
Phycisphaerae
Planctomycetia
Campylobacteria
Verrucomicrobiae
Gemmatimonadetes
UBA9160
Bacteroidia
Clostridia
Bacilli
Actinomycetes
Acidimicrobiia
Terriglobia
UBA6911
others
d
Transmembrane helices
seamount 12.17%
hadal trench 10.47%
abyssal plain 13.75%
cold seep 12.20%
hydrothermal vent 14.37%
Signal peptides
seamount 1.59%
hadal trench 1.17%
abyssal plain 3.14%
cold seep 0.70%
1.57%
hydrothermal vent

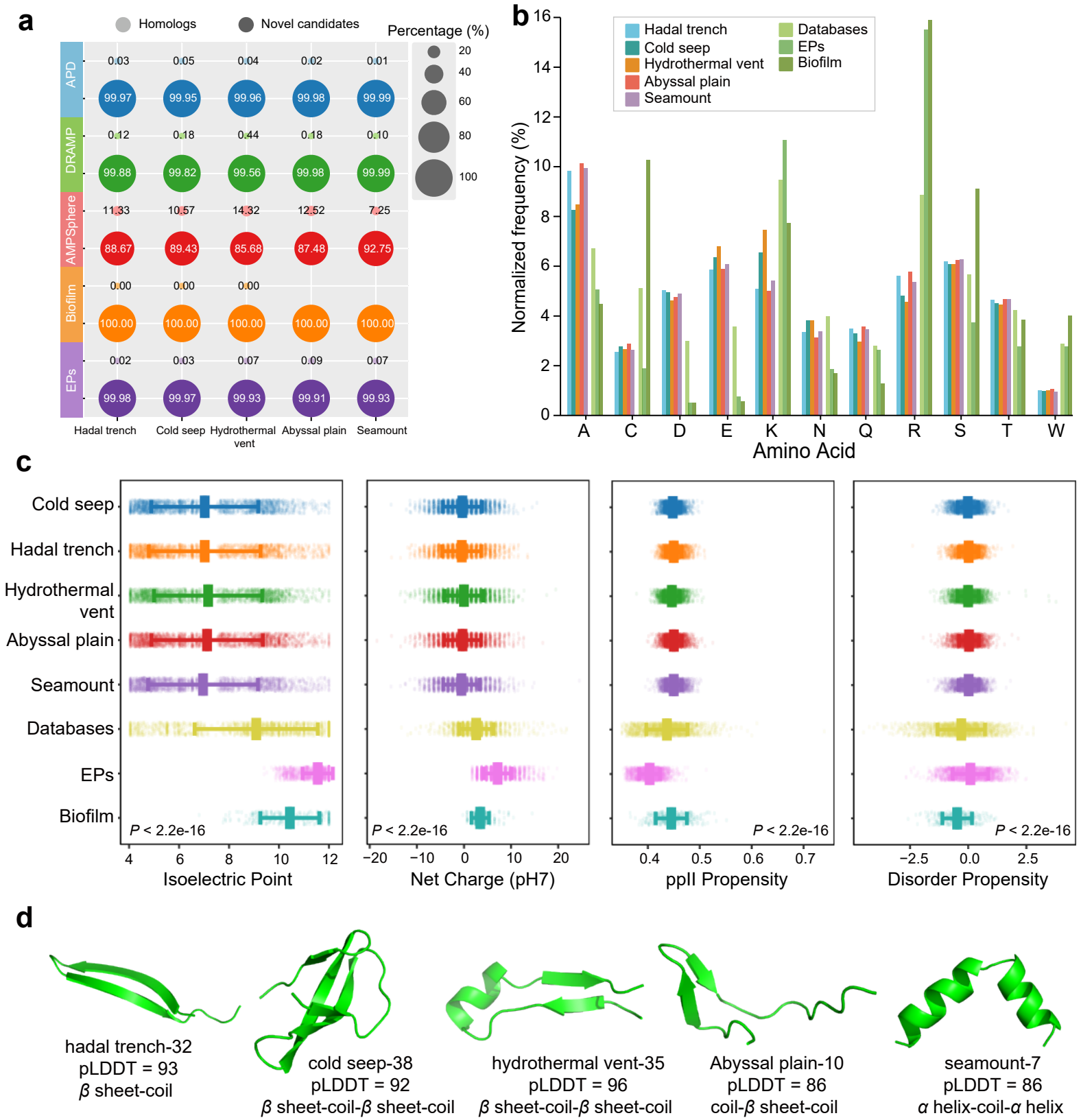
a
Homologs
Novel candidates
Percentage (%)
20
40
60
80
100
APD
DRAMP
AMPSphere
Biofilm
EPs
0.03 0.05 0.04 0.02 0.01
99.97 99.95 99.96 99.98 99.99
0.12 0.18 0.44 0.18 0.10
99.88 99.82 99.56 99.98 99.99
11.33 10.57 14.32 12.52 7.25
88.67 89.43 85.68 87.48 92.75
0.00 0.00 0.00
100.00 100.00 100.00 100.00 100.00
0.02 0.03 0.07 0.09 0.07
99.98 99.97 99.93 99.91 99.93
Hadal trench
Cold seep
Hydrothermal vent
Abyssal plain
Seamount
b
Hadal trench
Cold seep
Hydrothermal vent
Abyssal plain
Seamount
Databases
EPs
Biofilm
Normalized frequency (%)
Amino Acid
A C D E K N Q R S T W
c
Cold seep
Hadal trench
Hydrothermal vent
Abyssal plain
Seamount
Databases
EPs
Biofilm
P < 2.2e-16
Isoelectric Point
Net Charge (pH7)
ppII Propensity
Disorder Propensity
d
hadal trench-32
pLDDT = 93
β sheet-coil
cold seep-38
pLDDT = 92
β sheet-coil-β sheet-coil
hydrothermal vent-35
pLDDT = 96
β sheet-coil-β sheet-coil
Abyssal plain-10
pLDDT = 86
coil-β sheet-coil
seamount-7
pLDDT = 86
α helix-coil-α helix

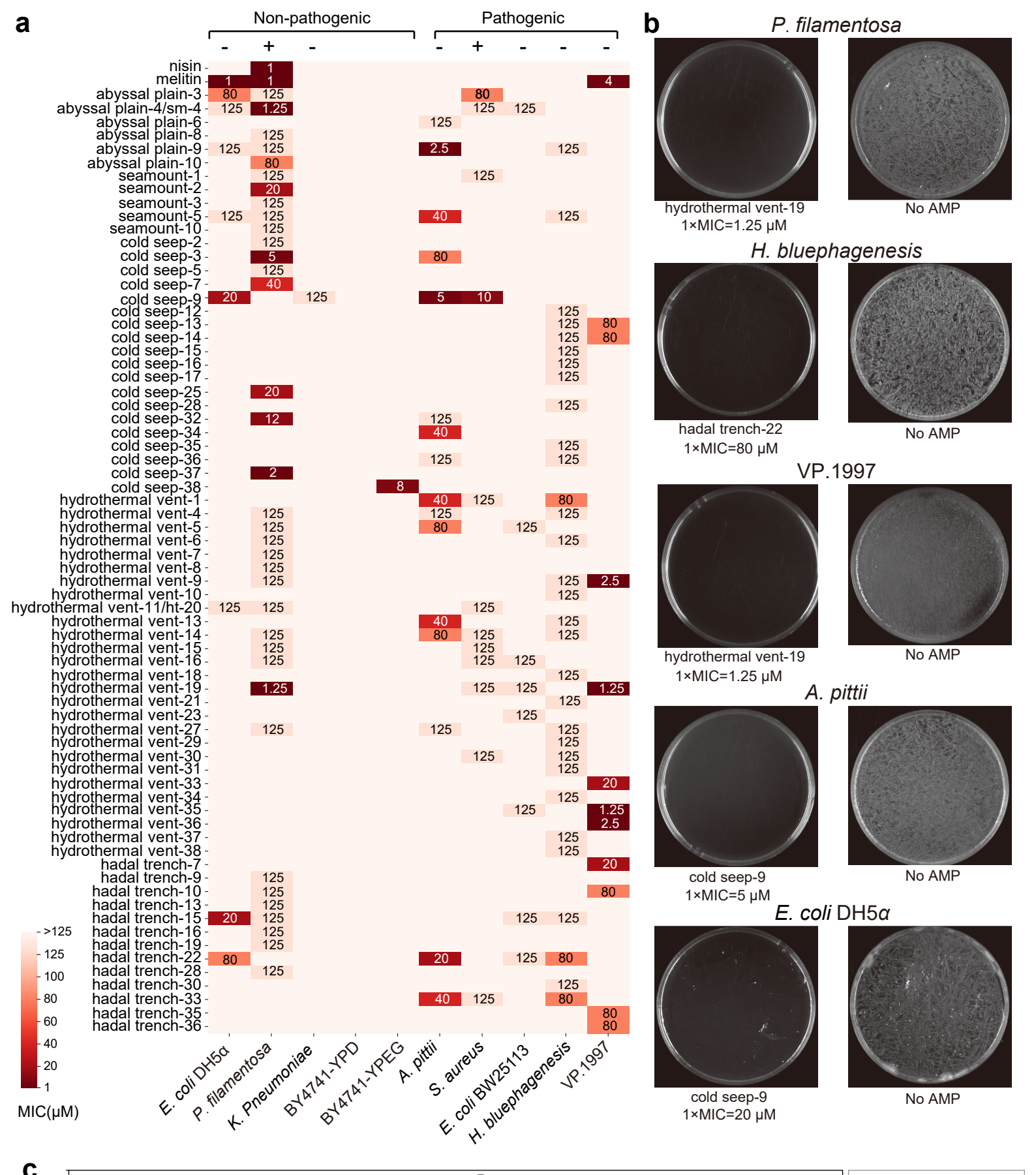
a
Non-pathogenic
Pathogenic
E. coli DH5α
P. filamentosa
K. Pneumoniae
BY4741-YPD
BY4741-YPEG
A. pittii
S. aureus
E. coli BW25113
H. bluephagenesis
VP.1997
MIC(μM)
>125
125
100
80
60
40
20
1
b
P. filamentosa
hydrothermal vent-19
1×MIC=1.25 μM
No AMP
H. bluephagenesis
hadal trench-22
1×MIC=80 μM
No AMP
VP.1997
hydrothermal vent-19
1×MIC=1.25 μM
No AMP
A. pittii
cold seep-9
1×MIC=5 μM
No AMP
E. coli DH5α
cold seep-9
1×MIC=20 μM
No AMP
c
Cell viability (%)
Hek293T
HepG2
Hela
hadal trench-22 1×MIC
hadal trench-22 2×MIC
cold seep-3 1×MIC
cold seep-3 2×MIC
cold seep-9 1×MIC
cold seep-9 2×MIC
cold seep-38 1×MIC
cold seep-38 2×MIC
hydrothermal vent-9 1×MIC
hydrothermal vent-9 2×MIC
hydrothermal vent-19 1×MIC
hydrothermal vent-19 2×MIC
hydrothermal vent-36 1×MIC
hydrothermal vent-36 2×MIC
abyssal plain-4/sm-4 1×MIC
abyssal plain-4/sm-4 2×MIC
No AMP
DMSO

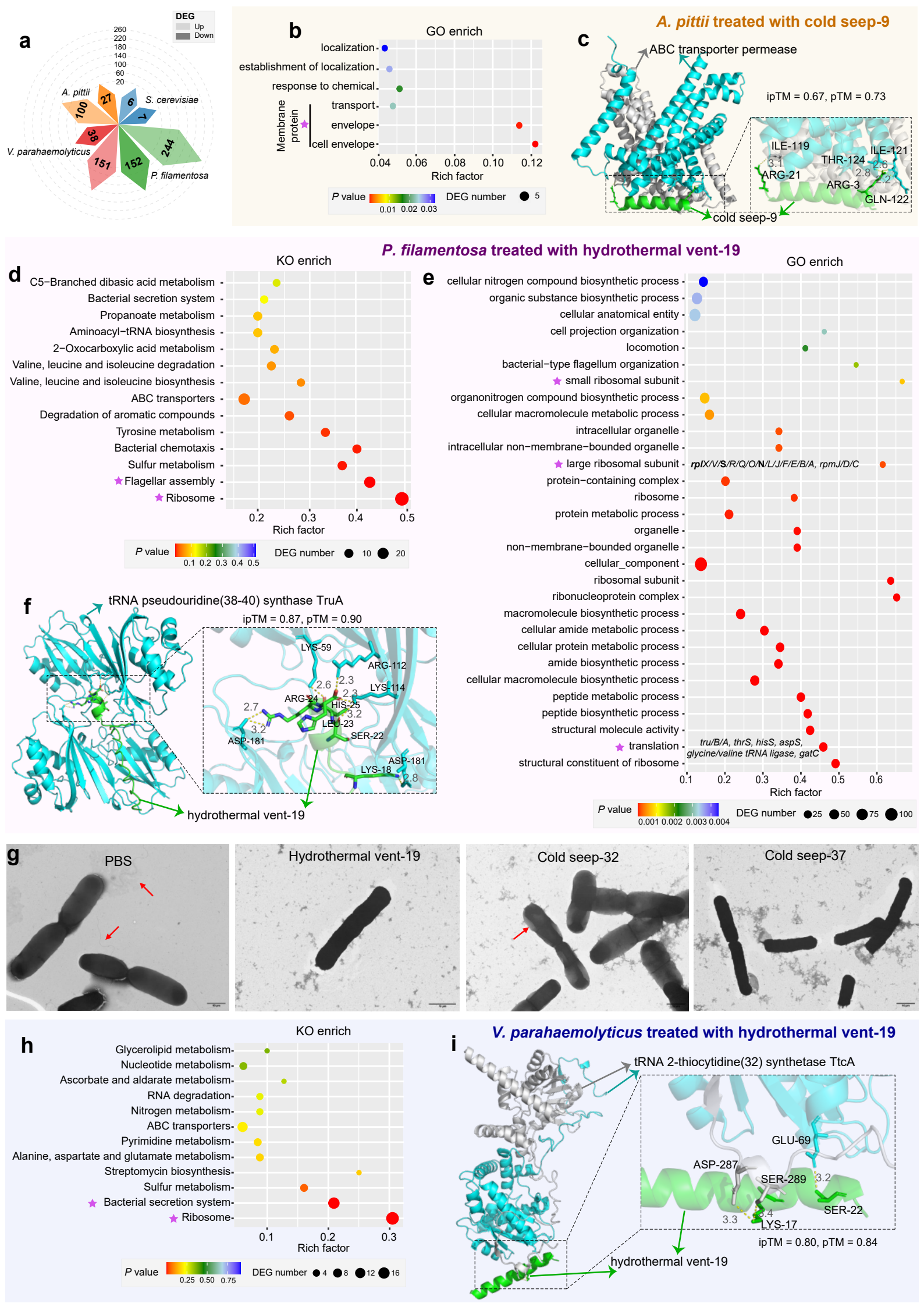
a
DEG
Up
Down
A. pittii
S. cerevisiae
V. parahaemolyticus
P. filamentosa
b
GO enrich
localization
establishment of localization
response to chemical
transport
envelope
cell envelope
Membrane protein
Rich factor
P value
DEG number
c
A. pittii treated with cold seep-9
ABC transporter permease
ipTM = 0.67, pTM = 0.73
ILE-119
ILE-121
THR-124
ARG-21
ARG-3
GLN-122
cold seep-9
P. filamentosa treated with hydrothermal vent-19
d
KO enrich
C5−Branched dibasic acid metabolism
Bacterial secretion system
Propanoate metabolism
Aminoacyl−tRNA biosynthesis
2−Oxocarboxylic acid metabolism
Valine, leucine and isoleucine degradation
Valine, leucine and isoleucine biosynthesis
ABC transporters
Degradation of aromatic compounds
Tyrosine metabolism
Bacterial chemotaxis
Sulfur metabolism
Flagellar assembly
Ribosome
Rich factor
P value
DEG number
e
GO enrich
cellular nitrogen compound biosynthetic process
organic substance biosynthetic process
cellular anatomical entity
cell projection organization
locomotion
bacterial−type flagellum organization
small ribosomal subunit
organonitrogen compound biosynthetic process
cellular macromolecule metabolic process
intracellular organelle
intracellular non−membrane−bounded organelle
large ribosomal subunit
rplX/V/S/R/Q/O/N/L/J/F/E/B/A, rpmJ/D/C
protein−containing complex
ribosome
protein metabolic process
organelle
non−membrane−bounded organelle
cellular_component
ribosomal subunit
ribonucleoprotein complex
macromolecule biosynthetic process
cellular amide metabolic process
cellular protein metabolic process
amide biosynthetic process
cellular macromolecule biosynthetic process
peptide metabolic process
peptide biosynthetic process
structural molecule activity
translation
tru/B/A, thrS, hisS, aspS, glycine/valine tRNA ligase, gatC
structural constituent of ribosome
Rich factor
P value
DEG number
f
tRNA pseudouridine(38-40) synthase TruA
ipTM = 0.87, pTM = 0.90
LYS-59
ARG-112
LYS-114
ARG-24
HIS-25
LEU-23
SER-22
ASP-181
LYS-18
hydrothermal vent-19
g
PBS
Hydrothermal vent-19
Cold seep-32
Cold seep-37
h
KO enrich
Glycerolipid metabolism
Nucleotide metabolism
Ascorbate and aldarate metabolism
RNA degradation
Nitrogen metabolism
ABC transporters
Pyrimidine metabolism
Alanine, aspartate and glutamate metabolism
Streptomycin biosynthesis
Sulfur metabolism
Bacterial secretion system
Ribosome
Rich factor
P value
DEG number
i
V. parahaemolyticus treated with hydrothermal vent-19
tRNA 2-thiocytidine(32) synthetase TtcA
GLU-69
ASP-287
SER-289
SER-22
LYS-17
ipTM = 0.80, pTM = 0.84
hydrothermal vent-19